Journal of Quantitative Spectroscopy & Radiative Transfer ▮ (▮▮▮▮) ▮▮▮–▮▮▮

Contents lists available at ScienceDirect

Journal of Quantitative Spectroscopy & Radiative Transfer

journal homepage: www.elsevier.com/locate/jqsrt

Review

Multiple-scattering in radar systems: A review

Alessandro Battaglia [a,b,*], Simone Tanelli [c], Satoru Kobayashi [d], Dusan Zrnic [e], Robin J. Hogan [f], Clemens Simmer [a]

[a] Meteorological Institute, University of Bonn, Bonn, Germany
[b] Earth Observation Science, Department of Physics and Astronomy, University of Leicester, Leicester, UK
[c] Jet Propulsion Laboratory, California Technology, 91101 Pasadena, CA, USA
[d] Applied Materials Inc., Santa Clara, CA, USA
[e] National Severe Storms Laboratory (NOAA), Norman, OK, USA
[f] Department of Meteorology, The University of Reading, Reading, UK

ARTICLE INFO

Article history:
Received 22 September 2009
Received in revised form
23 November 2009
Accepted 26 November 2009

Keywords:
Radar equation
Multiple scattering
Radiative transfer

ABSTRACT

Although extensively studied within the lidar community, the multiple scattering phenomenon has always been considered a rare curiosity by radar meteorologists. Up to few years ago its appearance has only been associated with two- or three-body-scattering features (e.g. hail flares and mirror images) involving highly reflective surfaces.

Recent atmospheric research aimed at better understanding of the water cycle and the role played by clouds and precipitation in affecting the Earth's climate has driven the deployment of high frequency radars in space. Examples are the TRMM 13.5 GHz, the CloudSat 94 GHz, the upcoming EarthCARE 94 GHz, and the GPM dual 13–35 GHz radars. These systems are able to detect the vertical distribution of hydrometeors and thus provide crucial feedbacks for radiation and climate studies. The shift towards higher frequencies increases the sensitivity to hydrometeors, improves the spatial resolution and reduces the size and weight of the radar systems. On the other hand, higher frequency radars are affected by stronger extinction, especially in the presence of large precipitating particles (e.g. raindrops or hail particles), which may eventually drive the signal below the minimum detection threshold. In such circumstances the interpretation of the radar equation via the single scattering approximation may be problematic. Errors will be large when the radiation emitted from the radar after interacting more than once with the medium still contributes substantially to the received power. This is the case if the transport mean-free-path becomes comparable with the instrument footprint (determined by the antenna beam-width and the platform altitude).

This situation resembles to what has already been experienced in lidar observations, but with a predominance of wide- versus small-angle scattering events. At millimeter wavelengths, hydrometeors diffuse radiation rather isotropically compared to the visible or near infrared region where scattering is predominantly in the forward direction. A complete understanding of radiation transport modeling and data analysis methods under wide-angle multiple scattering conditions is mandatory for a correct interpretation of echoes observed by space-borne millimeter radars.

* Corresponding author at: Earth Observation Science, Department of Physics and Astronomy, University of Leicester, Leicester, UK. Tel.: +44 116 2709859.
E-mail address: a.battaglia@le.ac.uk (A. Battaglia).

0022-4073/$ - see front matter
doi:10.1016/j.jqsrt.2009.11.024

Please cite this article as: Battaglia A, et al. Multiple-scattering in radar systems: A review. JQSRT (2010), doi:10.1016/j.jqsrt.2009.11.024

This paper reviews the status of research in this field. Different numerical techniques currently implemented to account for higher order scattering are reviewed and their weaknesses and strengths highlighted. Examples of simulated radar backscattering profiles are provided with particular emphasis given to situations in which the multiple scattering contributions become comparable or overwhelm the single scattering signal. We show evidences of multiple scattering effects from air-borne and from CloudSat observations, i.e. unique signatures which cannot be explained by single scattering theory. Ideas how to identify and tackle the multiple scattering effects are discussed. Finally perspectives and suggestions for future work are outlined.

This work represents a reference-guide for studies focused at modeling the radiation transport and at interpreting data from high frequency space-borne radar systems that probe highly opaque scattering media such as thick ice clouds or precipitating clouds.

Contents

1. Introduction

Although well-known in the lidar community, multiple scattering (*MS* hereafter) has always been regarded as a "rara avis" in the radar (radiowave detection and ranging) community. This is evident in radar books (e.g. [1,2]) when discussing the hypotheses underlying the radar equation, the basis for the interpretation of the radar signals. Therein many pages are dedicated to the extension of the reflectivity definition to large-compared-to-wavelength (the so-called "Mie") and to non-spherical scatterers, to the attenuation correction, to the antenna pattern and to the beam filling effects, and so on. It is seldom mentioned that the radar equation (as normally presented) hinges on the single scattering (*SS* hereafter) assumption, i.e. the reflected received power is assumed to come from radiation which has directly traveled from the transmitter to the scatterer and has been then back-scattered to the radar receiver (possibly being attenuated within the two-way path). The apparent backscatter β_{app}, which is directly proportional to the apparent radar reflectivity factor Z_{app}, measured at a range r, is then given simply by

$$\beta_{app}(r) = \beta_{eff}(r)\exp[-2\tau(r)] \quad (1)$$

where $\tau(r)$ is the total optical depth (inclusive of clouds, precipitation, and gas contributions) between the instrument and the position of the scatterer r, and β_{eff} is the "effective" backscatter of the medium (proportional to the effective reflectivity Z_{eff}). Note that Eq. (1) includes the trivial case of no attenuation, if the optical depth of the medium $\tau \ll 1$.

Please cite this article as: Battaglia A, et al. Multiple-scattering in radar systems: A review. JQSRT (2010), doi:10.1016/j.jqsrt.2009.11.024

The key assumption for the validity of Eq. (1) is that any scattered photon leaving the geometrical field of view (*FOV*) of the receiver is not detected, except those in the exact backscatter direction. Thus all possible successive orders of scattering contributions can be neglected. Such conditions are typically experienced by most of the currently operated radar systems (e.g. ground-based weather radars). After attenuation correction and elimination of spurious effects (like second trip echoes), the radar signal can be interpreted unambiguously as coming from a certain range and location, and the signal can be related to properties of the medium at that range and location. This is the basic principle underlying all active "ranging instruments".

Recent research oriented towards a better understanding of the water cycle and the role played by clouds and precipitation in affecting the Earth's climate has driven the deployment of high frequency (from 13 to 94 GHz) space-borne radars. A list of current and future space-borne radars with their specifics is provided in Table 1.

The precipitation radar (PR) at 13.8 GHz on board the tropical rainfall measuring mission (TRMM) satellite demonstrated the great potential of such instruments in detecting and characterizing the vertical structure of clouds and precipitation in the Tropics [3]. This information is crucial e.g. for deriving the vertical distribution of latent heat release [4]. Another significant step forward will be made by the *global precipitation measurement* (*GPM*, http://gpm.gsfc.nasa.gov/), with critical ameliorations in the radiometer and radar systems compared to the corresponding instruments flown on the TRMM satellite. The GPM radar system will include two radars at different frequencies, i.e. 13.6 and 35 GHz. These instruments will mitigate the well known problem of having to specify a priori the drop size distribution of the precipitation.

CloudSat, launched in April 2006 [5], paved the way to space-borne nadir-pointing 94 GHz cloud radars as unique precipitation detectors, suited for better understanding the transition between non-precipitating and precipitating clouds. These radars detect drizzle (e.g. [6]), light rain or snowfall, thus offering a unique and more holistic view of the water cycle. Even information on the vertical structure of hurricanes has been inferred ([7] and refer to the CloudSat web-page http://cloudsat.atmos.colostate.edu/ for wide variety of examples). Interestingly even for such heavy precipitating systems the complete attenuation of the signal seems to occur much less often than expected.

As a follow-up, the European Space Agency selected the Earth, Clouds, Aerosols, and Radiation Explorer (*EarthCARE*) mission with a space-borne 94 GHz radar (launch intended in 2013). Thanks to its improved sensitivity and additional *Doppler capabilities*, the EarthCARE cloud-radar will provide vertical velocity profiles to further characterize the upper layers of convective cells and of some moderately convective systems with pronounced ice sedimentation. Thus EarthCARE will further enhance our ability to monitor and study cloud and precipitation processes on a global scale. Finally we mention the Aerosol/Cloud/Ecosystem (ACE) mission, which has been proposed in the U.S. National Research Council Decadal Survey as one of the 17 space missions recommended for the next decade. Among other instruments, ACE will carry a 94 and possibly a 35 GHz radar, with cross-track scanning and Doppler capabilities. The latter option is currently being studied at NASA.

As the frequency of operations and the distance from the observed medium increase, some factors come into play which have the potential to enhance the significance of higher order of scattering in the radar echo and hence to break the validity of the *SS* approximation.

- *The increase in the optical thickness of the medium* enhances the probability of interaction of radiation within the medium. As a rule of thumb, the critical condition to activate considerable *MS* contributions is the decrease of the mean free-radiation path (defined as the inverse of the extinction coefficient) towards values comparable or smaller than the radar footprint dimension (which can be of the order of few kilometers for typical space-borne systems).
- *The increase of scattering versus absorption cross-section*, i.e. the *SS* albedo $\tilde{\omega}$, allows the radiation to interact many times within the medium before being absorbed or leaving the cloud and eventually being redirected to the receiver.
- *The change of hydrometeors scattering phase functions*, that become more peaked in the forward direction, tends to keep the radiation within the instrument *FOV* despite scattering, thus increasing the contribution of higher orders of scattering.

A vertical cut of the 3D resolved cloud hydrometeor content simulated for a hurricane system [8] is presented in Fig. 1. The relevant *SS* properties (extinction coefficient k_{ext}, albedo $\tilde{\omega}$ and asymmetry parameter g, defined as the average cosine of the scattering phase function: $g = \langle \cos\theta \rangle$) at 13.5 and 94 GHz for such scenario are depicted in Fig. 2. This model case represents an extreme

Table 1
Characteristics of space-borne radars for current and future missions.

Mission name	Radar frequency (GHz)	Radar band	Satellite altitude	Radar beamwidth	Horizontal resolution	Best MDT
TRMM	13.8	K_u	350 km	$0.71^\circ \times 0.71^\circ$	4.3 km	17 dBZ
GPM	13.8	K_u	400 km	$0.7^\circ \times 0.7^\circ$	4.9 km	17 dBZ
GPM	35.5	K_a	400 km	$0.7^\circ \times 0.7^\circ$	4.9 km	15 dBZ
CloudSat	94.0	W	705 km	$0.1^\circ \times 0.1^\circ$	1.2 km	−30 dBZ
EarthCARE	94.0	W	395 km	$0.08^\circ \times 0.08^\circ$	0.8 km	−36 dBZ
ACE	94.0	W/K_a	*TBD*	*TBD*	*TBD*	*TBD*

Please cite this article as: Battaglia A, et al. Multiple-scattering in radar systems: A review. JQSRT (2010), doi:10.1016/j.jqsrt.2009.11.024

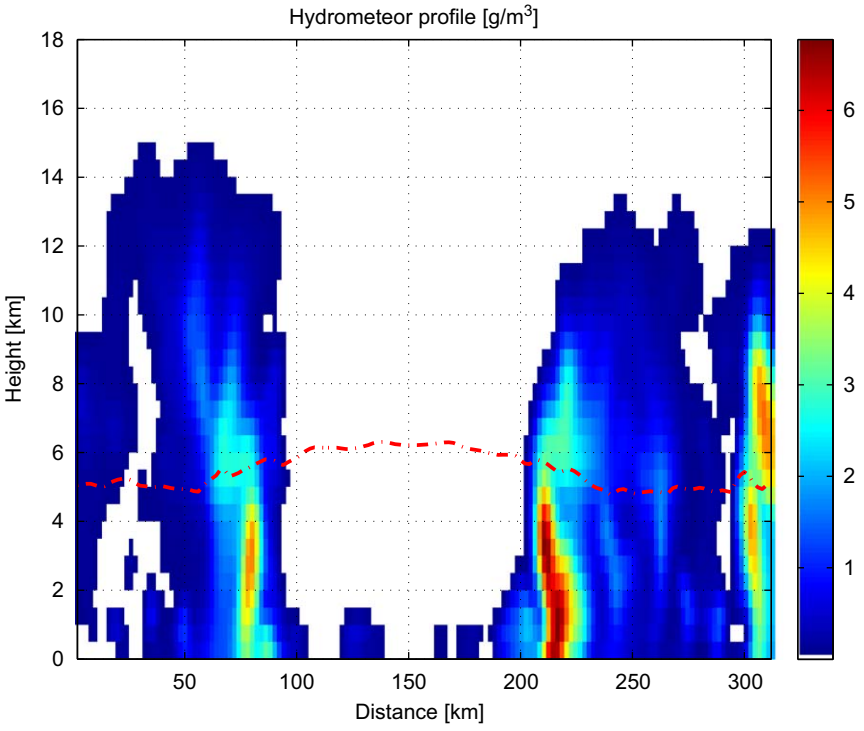

Fig. 1. Vertical cross-section of the total hydrometeor content in g/m^3 simulated by the GCE-CRM for a hurricane system. The red dashed line indicates the freezing level height. The eye of the hurricane is clearly visible in the middle. (For interpretation of the references to color in this figure legend, the reader is referred to the web version of this article.)

scenario, with hydrometeor contents exceeding $6\,g/m^3$ in the precipitating core located at about 220 km. The extinction properties mirror the hydrometeor content with the lower frequency having values much smaller than those achieved at 94 GHz. At the two frequency values as high as 2.2 and $12.5\,km^{-1}$ are encountered, which correspond to a mean-free-path equal to 450 and 80 m, and to extreme one-way attenuation coefficients equal to 9.5 and 54 dB/km, respectively. In addition to the large difference in the amplitude of the extinction coefficients of the medium at the two frequencies, the precipitating medium has much less absorption at 94 GHz: the cloud above the freezing level, where large ice particles are present, has $\tilde{\omega}$ above 0.8 while the heavily precipitating rain region is characterized by values close to 0.5. On the other hand, at 13.5 GHz absorption dominates scattering, especially when liquid phase hydrometeors are present. This reflects the behavior of *SS* ice and water particle properties (e.g. see [9, Chapter 3]). Finally, while at 13.5 GHz the medium appears to scatter almost isotropically ($-0.1 \le g \le 0.1$ with raindrops/ice particles slightly producing more/less backscattering), at 94 GHz the forward scattering dominates with large ice particles capable of producing g values as high as 0.7.

When comparing these mean-free-path values with the footprint of space-borne radars (sixth column in Table 1) this example hints that *MS* effects should be relevant at a frequency somewhere between 13 GHz (the operating frequency of the old generation of space-borne radars) and 35 GHz (the lowest frequency of the new generation of radars). Therefore, a detailed investigation of *MS* effects for radar systems at frequencies in the mm region is a timely endeavor.

1.1. Multiple scattering regimes

The *MS* phenomenon in active remote sensing has been thoroughly studied by the lidar community (see [10,11] and references therein). It is enlightening to distinguish two *MS* regimes experienced by active remote sensors (see [12,13]).

1. *Small-angle multiple scattering*: For lidar application, cloud particles are typically much larger than the wavelength; hence Babinet's principle states that half of the extinguished energy is scattered into a narrow forward lobe with a $1/e$ half-width of $\Theta = \lambda/(\pi a)$, where λ is the wavelength and a is the radius of the particle (details in [14]). These small angle forward-scattered photons may remain within the *FOV* of the detector (lidar *FOV* s are within the range of 0.1–5 mrad) and contribute to the apparent backscatter (e.g. red path in the top panel of Fig. 3). Photons that experience wide-angle scattering will leave the *FOV* and they will not be detected (e.g. green path in Fig. 3).
   The condition for this to occur is

$$\frac{l\Theta}{\tilde{\omega}} \le X \ll l_t \tag{2}$$

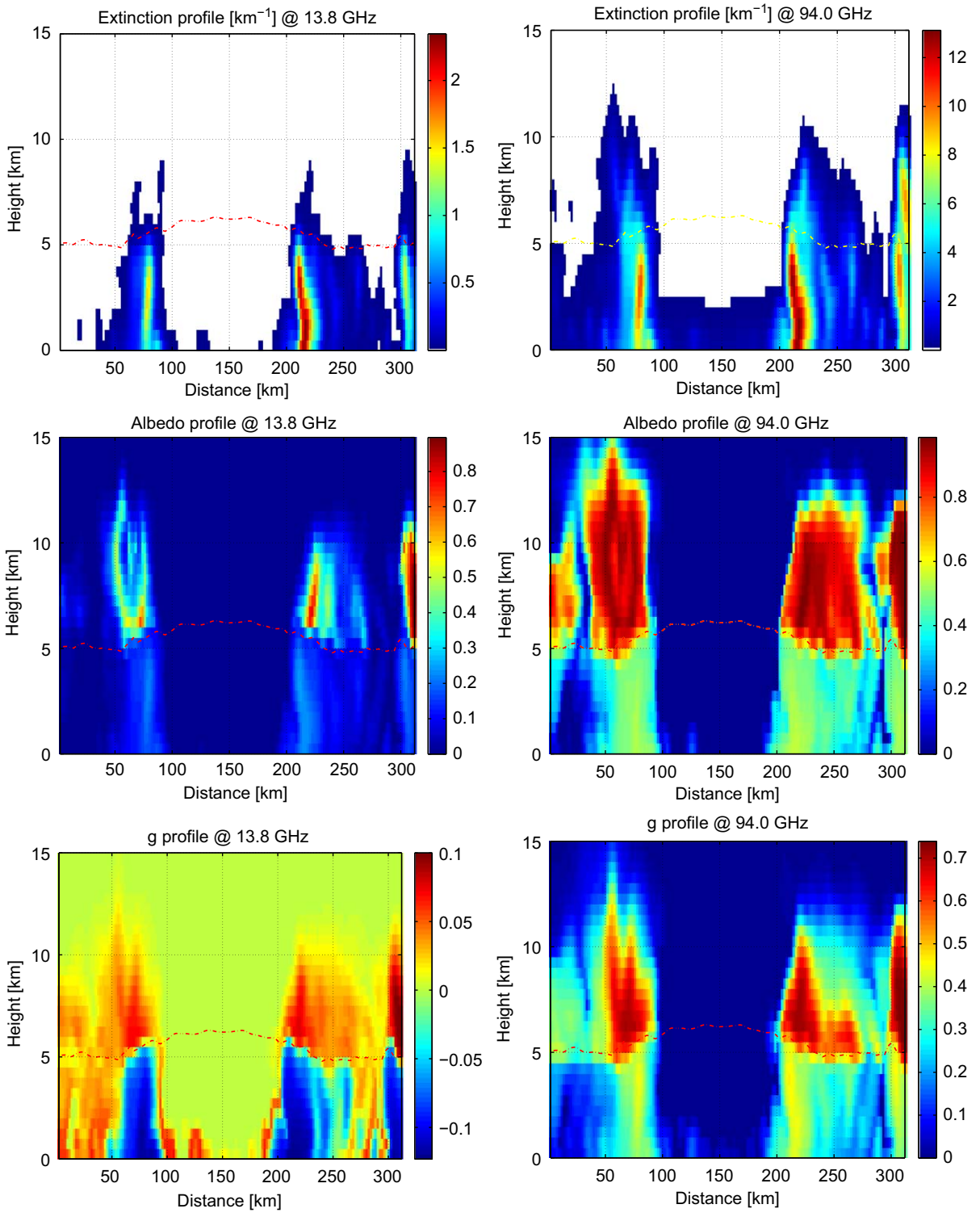

Fig. 2. Vertical cross-section of the extinction coefficient k_{ext} in km^{-1} (top), the *SS* albedo (middle) and the asymmetry parameter g (bottom) for the hurricane precipitating system, whose hydrometeor content is depicted in Fig. 1. The *SS* properties refer to 13.5 GHz (left) and to 94.0 GHz (right panels). The dashed line indicates the freezing level height.

Please cite this article as: Battaglia A, et al. Multiple-scattering in radar systems: A review. JQSRT (2010), doi:10.1016/j.jqsrt.2009.11.024

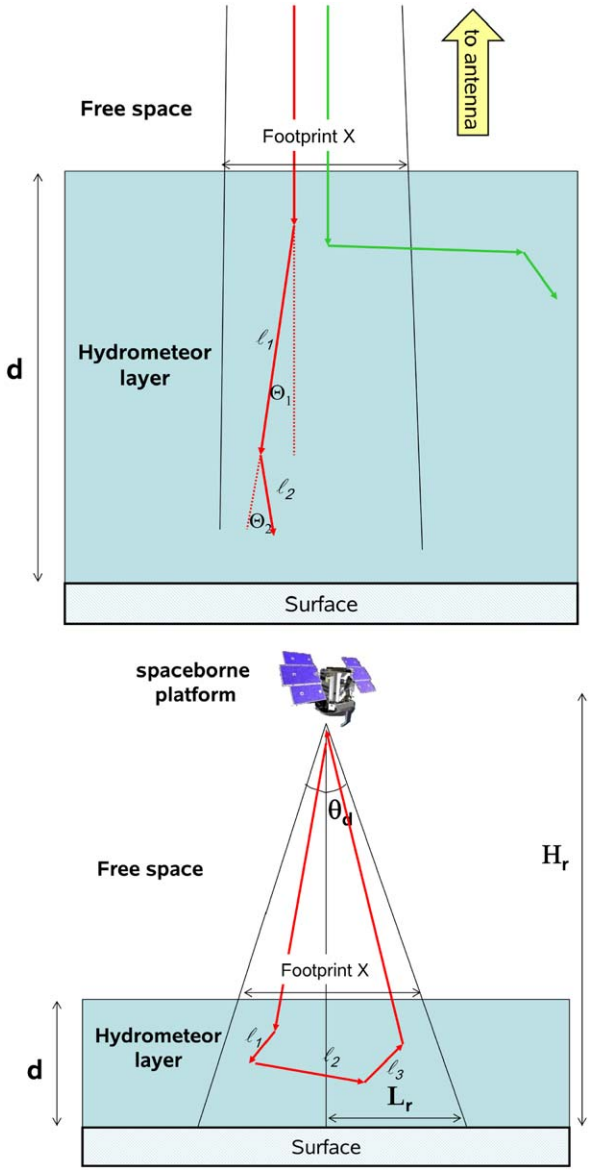

Fig. 3. Schematic representing two *MS* regimes. Radiation released from the active sensor at the top of the scene enters the scattering medium (blue shaded area) and undergoes small-angle (top panel) and wide-angle (bottom panel) scattering. Contributions to the received power are relevant only when coming from radiation interacting within the antenna footprint (marked by the black lines).

where X is the width of the "footprint" of the receiver at the range of the scatterers (see Fig. 3), $l=1/k_{ext}$ is the mean-free-path and $l_t=l/[\tilde{\omega}(1-\tilde{\omega}g)]$ is the "transport mean-free-path" [15].

2. *Wide-angle multiple scattering*: If the footprint size X is on the same order or larger than l_t (bottom panel in Fig. 3)

$$X \gtrsim l_t \tag{3}$$

wide-angle scattered photons may remain within the *FOV* and eventually they may be detected.

In radar systems the first *MS* regime never materializes since hydrometeors have sizes smaller or at most comparable to the radar wavelength. Vice versa, given the hydrometeors' more isotropic-like scattering pattern, the second regime might be encountered.

1.2. Multiple scattering: signal or noise?

Small and wide-angle *MS* produce two completely different interpretation paradigms when considering the instrument ranging capability. For all ranging active instruments the radiation's time of return is assumed proportional to the straight-line, round-trip distance between the scattering volume and the collocated transmitter/receiver assembly. Ideally active remote sensing only detects *SS*; thus the straight line assumption is satisfied and the sample volume responsible for backscattering the transmitted radiation is ranged precisely in space. Radiation may, however, encounter a large number of scattering interactions. With each successive scatter, the residence time of radiation within the medium is increased; depending on the extended residence time of such multiply scattered radiation, its energy may be mapped to range locations at considerably larger distances from the sample volume in which primary scatter occurred. Once *MS* contributions to the return signal become significant, the ranging capability of the instrument deteriorates differently (as outlined hereafter) for the two mentioned *MS* regimes.

The distance traveled by photons that have only undergone *small-angle MS* is approximately the same as that of *SS* photons; thus the time of travel can still be converted unambiguously into the distance of the backscattering medium. This component is sometimes referred to as "correctly ranged" *MS* return. The total return is enhanced (see dashed line in Fig. 4) and its interpretation should not be based on Eq. (1). The assumption that the scattering events occur in the forward direction allows for a closed form of a multiple-scattering equation for lidar [16,10]. In practice, small-angle *MS* enhances the penetration of the cloud and hence serves as an aid producing an exploitable signal in the retrieval of cloud vertical structure.

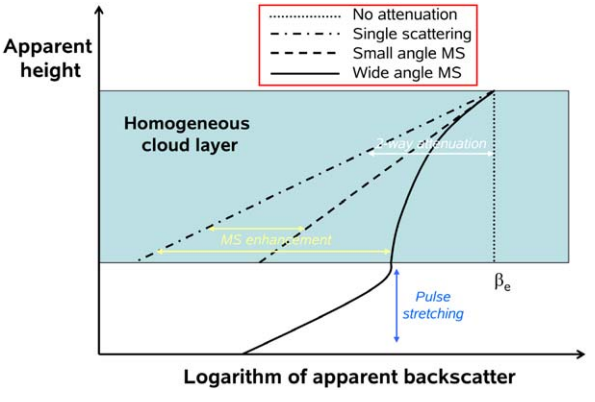

Fig. 4. Apparent backscatter that a nadir-looking instrument would observe in a homogeneous slab of cloud for different scattering regimes that active sensors encounter (adapted from [13]).

Please cite this article as: Battaglia A, et al. Multiple-scattering in radar systems: A review. JQSRT (2010), doi:10.1016/j.jqsrt.2009.11.024

When dealing with *wide-angle MS* we have to contend with the difficulty that the associated time delay makes returning radiation appear to originate from a range beyond the distance to which it actually penetrated. Radiation does not necessarily penetrate to the depths indicated by the raw return and thus there is no way to retrieve properties relative to such depths from the sensor signal. In the presence of a cloud/rain layer this translates into a "pulse stretching" well beyond the layer base as illustrated in Fig. 4 (continuous line). This feature is also visible in large footprint (of the order of 1 km) space-borne lidar observations of liquid water clouds where it appears as streaks of fading intensity below the cloud base (see the LIdar Technology Experiment (LITE) [17]). Such effects are not noticeable in lidar observations made with smaller footprints (of the order of 100 m) like with CALIPSO and IceSAT [18]. With radar systems it appears in the form of hail spikes and mirror images (see discussion in Section 3) and in exceptional long tails apparently coming even from below the surface in CloudSat 94 GHz radar observations of deep tropical convective precipitation [19] and Section 6. More problematic cloud/rain profile returns may contain in-cloud/rain pulse stretching, which contaminates the *SS* return such that detailed profile information is lost entirely. In this case the presence of *MS* can be regarded more as noise than as signal, causing the loss of the ranging capability and further complicating any retrieval procedure.

2. Introducing multiple scattering in the radar equation

The classical radar equation (e.g. see [1,2]) is usually based on the assumption that the apparent reflectivity is only determined by *SS* contributions. Following [20] we will briefly summarize how to generalize the radar equation to include *MS* components. In particular a new generalized definition of the radar reflectivity, in terms of backscattered specific intensity, is introduced.

Let us consider a radar with radial resolution $\Delta r \equiv c\tau/2$ (τ being the pulse width, c the speed of light) transmitting a power P_T (Fig. 5). Let us suppose an observation geometry, where the radar is placed in the origin. For simplicity of notation, we introduce a slant reference coordinate system $(r', \overline{\theta}, \overline{\varphi})$ with its vertical coordinate coincident with the radar range r along the pointing angle $\Omega_0 = (\theta_0, \varphi_0)$. The corresponding solid angle $\Omega_r = (\overline{\theta}, \overline{\varphi})$ stands for the angle between r and r'. The power density $F_T(r)$ impinging at range r in a given direction, opposite to the receiving direction $\hat{\Omega}_r$, is related to P_T through the antenna gain function $G(\hat{\Omega}_r)$ by

$$F_T(r) = \frac{P_T}{4\pi r^2} G(\hat{\Omega}_r) \tag{4}$$

Very often the antenna gain function is normalized (g_n) to its maximum value G_0 (which is typically obtained along the antenna axis) as: $g_n(\hat{\mathbf{\Omega}}) \equiv G(\hat{\mathbf{\Omega}})/G_0$. From this variable two useful integral quantities can be derived: the antenna pattern solid angle Ω_p and the two way main-lobe solid angle Ω_{2A}

$$\Omega_p \equiv \int g_n(\hat{\mathbf{\Omega}})\, d\Omega, \quad \Omega_{2A} \equiv \int [g_n(\hat{\mathbf{\Omega}})]^2\, d\Omega \tag{5}$$

For instance a Gaussian antenna pattern with a 3-dB beamwidth θ_d is described by

$$g_n(\theta) = \exp\left[-4\ln 2\left(\frac{\theta^2}{\theta_d^2}\right)\right] \tag{6}$$

θ being the polar zenith angle relative to the antenna axis. The $3-dB$ footprint radius at the ground is approximated by $L_r \equiv H_r \tan(\theta_d/2)$ (see Fig. 3, H_r is the radar height) while the antenna pattern solid angle Ω_p equals $\pi\theta_d^2/4\ln 2$ and the two way main-lobe solid angle Ω_{2A} equals $\pi\theta_d^2/8\ln 2$.

The transmitted power P_T is partially reflected back by each particle intercepting the radar beam within the scattering volume. The radar equation provides the received power as a function of the radar and the medium characteristics. The mean apparent (or effectively measured) received power due to the scattering volume ΔV_r with range resolution Δr at distance r in the presence of *MS* can be generally expressed as an integral of the received specific intensity (measured in $W/(m^2\,sr)$) from apparent ranges between $r-\Delta r/2$ and $r+\Delta r/2$, $\langle I_{app}(r, \hat{\mathbf{\Omega}})\rangle_{\Delta r}$, weighted by the antenna effective area $A(\hat{\mathbf{\Omega}})$ over the solid angle [21]:

$$\begin{aligned}\langle P_{Rec}(r, \Omega_0)\rangle &= \int_{4\pi} A(\hat{\mathbf{\Omega}})\langle I_{app}(r, \hat{\mathbf{\Omega}})\rangle_{\Delta r}\, d\Omega \\ &= \frac{\lambda^2}{4\pi}\int_{4\pi} G(\hat{\mathbf{\Omega}})\langle I_{app}(r, \hat{\mathbf{\Omega}})\rangle_{\Delta r}\, d\Omega\end{aligned} \tag{7}$$

where we have related the antenna gain G to the antenna effective cross-section A through the reciprocity formula ($A = \lambda^2/(4\pi)G$). The expression (7) is general and simply states that $\langle I_{app}(r, \hat{\mathbf{\Omega}})\rangle_{\Delta r}$ is the key unknown quantity to be computed. The received specific intensity is obtained by summing up terms with different scattering order as

$$\langle I_{app}(r, \hat{\mathbf{\Omega}})\rangle_{\Delta r} = \sum_j \langle I^{[j]}_{app}(r, \hat{\mathbf{\Omega}})\rangle_{\Delta r} \tag{8}$$

The only feature common to all terms present in the right hand side of Eq. (8) is the traveled total radiation path, which is within the interval $[2r-\Delta r, 2r+\Delta r]$.

The radar equation in the *SS* approximation is usually expressed in terms of the single scattering (*SS*) apparent radar reflectivity $Z^{[1]}_{app}$ as [22,2]

$$\begin{aligned}\langle P^{[1]}_{Rec}(r)\rangle &= A_{e0}\int_{4\pi} g_n(\hat{\mathbf{\Omega}}) I^{[1]}_{app}(r, \Delta r, \hat{\mathbf{\Omega}})\, d\Omega \\ &= \frac{A_{e0}G_0\Omega_{2A}\Delta r}{(4\pi)^2}\frac{P_T}{r^2}\frac{\pi^5|K_w|^2}{\lambda^4} Z^{[1]}_{app}(r)\end{aligned} \tag{9}$$

where $G_0 = 4\pi/\Omega_p$ and $A_{e0} = (\lambda^2/4\pi)G_0$ are the maximum directive gain and maximum antenna aperture, respectively, λ is the radar wavelength. Ω_{2A} is the two way main-lobe solid angle defined in Eqs. (5). The $|K_w|^2$ is the dielectric factor usually assumed for liquid water. Some calibration conventions use its value at centimeter wavelengths, 0.93, whereas others use the value at the frequency in use, but it should be noted that at millimeter wavelengths this quantity is temperature dependent. For instance for CloudSat frequency $|K_w|^2$ is set equal to 0.75, i.e. the dielectric factor for liquid water at 94 GHz and 10 °C. Note that Eq. (9) further simplifies for Gaussian antenna patterns ($G_0\Omega_{2A} = 2\pi$) and for pencil beam antennas ($G_0\Omega_{2A} = 4\pi$).

Please cite this article as: Battaglia A, et al. Multiple-scattering in radar systems: A review. JQSRT (2010), doi:10.1016/j.jqsrt.2009.11.024

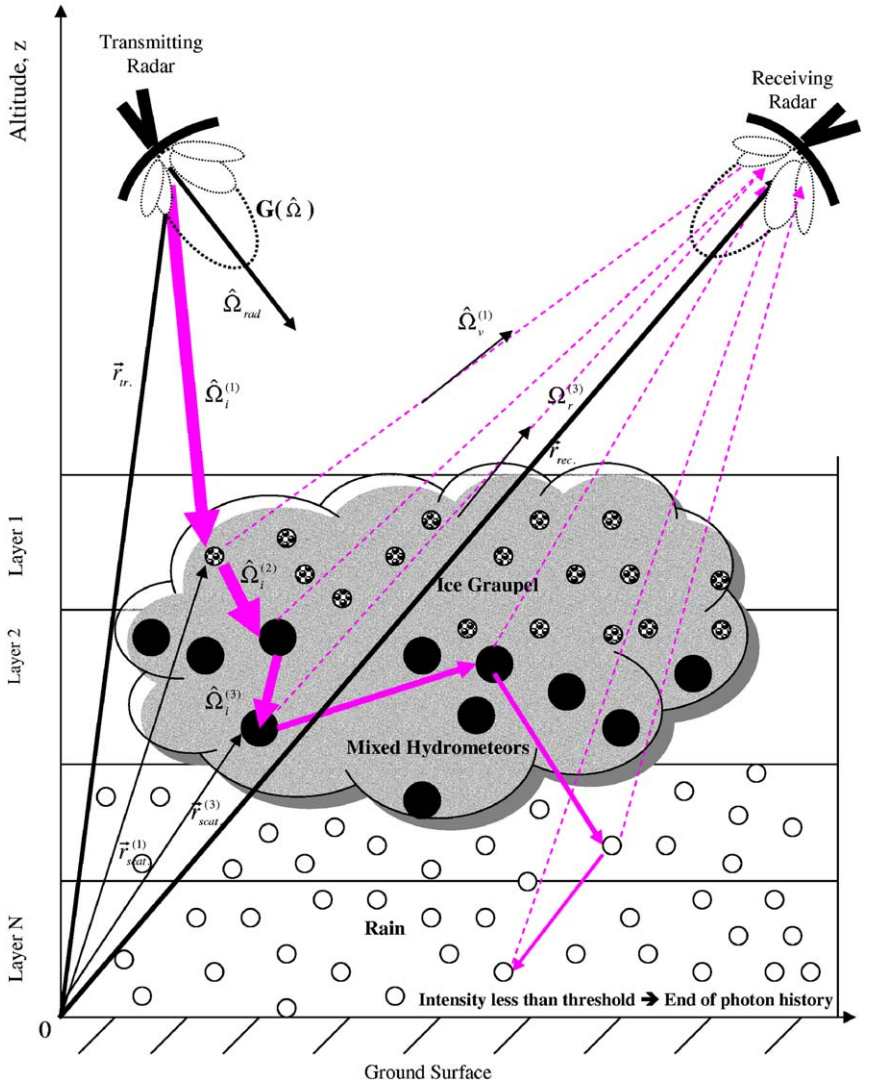

Fig. 5. Geometry and principles to compute the radar *MS* apparent reflectivity Z_{app}^{MS}. Extracted from [24].

In Eq. (9) all the scattering medium properties are characterized by the apparent reflectivity, which can be related to the effective reflectivity factor Z_{eff} by

$$Z_{app}^{[1]}(r) \equiv Z_{eff}(r)\underbrace{e^{-2\int_o^r k_{ext}(\xi)\,d\xi}}_{A_{2-way}(r)} = \underbrace{\left[\frac{\lambda^4}{\pi^5|K_w|^2}\overbrace{\int_D \sigma_{back}(D)N(D)\,dD}^{k_{back}(r)}\right]}_{Z_{eff}(r)} A_{2-way}(r) \qquad (10)$$

with σ_{back} the backscattering cross-section, D the diameter of the scatterers and $N(D)$ the size distribution of the scatterers (per unit volume and unit diameter interval) within the radar resolution volume. Eq. (10) implicitly defines also the two-way attenuation $A_{2-way}(r)$ (typically expressed in dB/km) and the radar backscattering coefficient k_{back} (in m^{-1}) at range r. Keep in mind that, outside the radar community the backscattering coefficient is usually denoted by the symbol β [e.g. here in Eq. (1)] in units $m^{-1}\,sr^{-1}$. Its relation to the radar backscattering coefficient is: $\beta_{back} = k_{back}/(4\pi)$ [23, Section 4.6].

By comparing Eq. (7) and (9), it is straightforward to introduce an apparent reflectivity of order [j] (see details in [24]):

$$Z_{app}^{[j]} \equiv \left[\frac{\Omega_p \int_{4\pi} g_n(\hat{\boldsymbol{\Omega}}) I_{app}^{[j]}(r, \Delta r, \hat{\boldsymbol{\Omega}}) r^2\, d\Omega}{\Omega_{2A} P_T}\right] \frac{4\pi}{\Delta r}\,\frac{\lambda^4}{\pi^5|K|^2} \qquad (11)$$

which is the mean value of the apparent received specific radiation intensity, which has been scattered j times within the medium.

Eq. (11) can be easily generalized to include polarization by substituting the scalar intensity I_{app} with the

Please cite this article as: Battaglia A, et al. Multiple-scattering in radar systems: A review. JQSRT (2010), doi:10.1016/j.jqsrt.2009.11.024

Stokes vector $\bar{\mathbf{I}}_{app}$. Hereafter, particular emphasis is put on copolar and cross-polar (subscript *co* and *cx*, respectively) reflectivities; for instance $Z_{cx}^{[2]}$ will indicate the fraction of the second order of scattering reflectivity, which is cross-polarized, with respect to the transmitted signal.

3. Three body scattering: the forerunner of *MS* effects

Phenomena comprising three-body scattering with at least one of these bodies involving a highly reflecting surface have already been identified to produce specific radar echoes. The most striking ones are hail spikes in ground-based weather radars and mirror images in space and airborne radars.

3.1. Hail spikes

The hail spike signature refers to an appendage seen in weather radar displays of reflectivity behind hail bearing storm cells. It was explained and quantified by [22] in terms of multiple scattering between hydrometeors and the ground. Although the signature is routinely used by the US National Weather Service forecasters for warnings, only four published studies in scientific literature address its physical basis [25–28]. The explanation is as follows: the transmitted EM wave is scattered by large hydrometeors towards the ground. The ground backscatters the wave to the hydrometeors which in turn scatter it back to the radar antenna. Because of this, the phenomenon is referred to as "three body scattering". Zrnic [22] derived the radar equation for the signature as a function of the distance r between the hail shaft and the reflecting ground, and he demonstrated excellent agreement with observation. The theory considers the case $r > d+h$, where d is the radial extent of the hail shaft and h is the height of the beam above ground intercepting the shaft. Zrnic's data were from a 10 cm wavelength radar and he attributed the contribution to non-Rayleigh scattering by large wet hail. Wilson and Reum [25] made a thorough analysis of several "three body scattering phenomena". They included cases where $r < d+h$, and considered 3 and 5 cm radar wavelengths as well. Furthermore they documented examples from Alabama that exhibited three body scattering signatures with no hail reaching the ground. Lemon [26] presents observations of three body scattering signatures (*TBSS*) made with the WSR-88D (Weather Surveillance Radar, 1988, Doppler). Although all storms reported in that study produced hail larger than 6.5 cm in diameter, the article implies that this artifact requires a hail diameter above 2.5 cm. They also stressed the predictive value of the *TBSS* because it is created aloft and typically precedes surface hail fall and strong winds by 10–30 min. In a recent article, [28] reports observations of weak *TBSS* with the WSR-88D in Texas and South Dakota. Such *TBSS* observations from this network were only possible, when reflectivity threshold were lowered from 5 to −5 dB*Z*. The storms associated with these weak *TBSS* produced hail up to 25 mm in size and had primary reflectivity values above 56 dB*Z*. Typical *TBSS* reflectivity factors were in the range between −5 and 4 dB*Z*; the lowest observed was at −14 dB*Z*.

Hubbert and Bringi [27] realized that the bidirectional reflections would add to the returned power. It appears that these authors added power (like [22]) rather than the coherent voltage (fields) contributions in their derivations. Nonetheless, this omission had no bearing on the results in either of the papers because both use relative power values; in [22] the dependence on r is relative to the maximum of the reflectivity core, whereas in [27] the differential reflectivity (ratio of powers for horizontal and vertical polarizations) are computed. We reexamine the radar equation for the three body scattering, correct it for the omission of the coherent sum, and present recent examples of the signature.

3.1.1. Radar equation for 3-body scattering

Fig. 6 depicts the volume within the beam wherein scattering is assumed to be sufficiently strong to produce a detectable three body signature. Let the range extent of this volume be d (typically few kilometers). The beam travels from the antenna to the hail stone (R_i), then from hail to the ground (r_i), scatters from the ground (r_j) back to another hailstone at R_j and then to the antenna. It is important to note that the same path, but in opposite direction (marked with opposite arrows in Fig. 6), may be taken by the electromagnetic waves, and that both contributions *add coherently* at the antenna, a fact

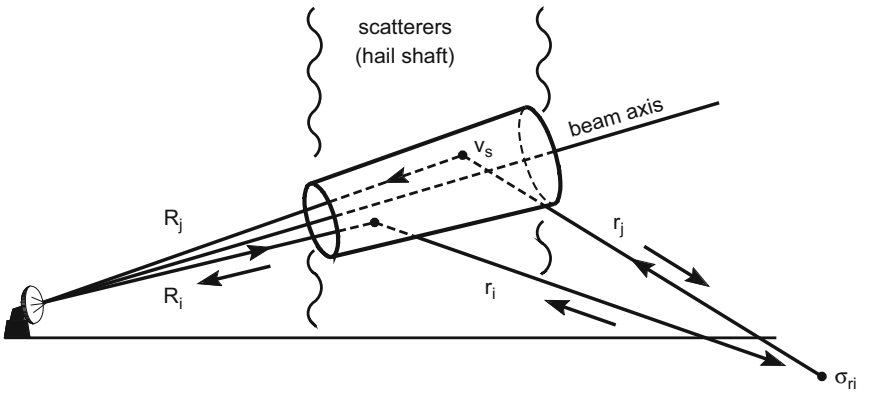

Fig. 6. The three body scattering process. The bidirectional path comprising the radar, the *i*th and *j*th scatterer, and the ground is indicated.

Please cite this article as: Battaglia A, et al. Multiple-scattering in radar systems: A review. JQSRT (2010), doi:10.1016/j.jqsrt.2009.11.024

omitted in [22]. Since the phases of the electric fields related to these two wave-paths are exactly in phase, the corresponding total intensity will be twice as much the sum of the intensity associated with each single field (see also Fig. 13 and related discussion).

For one pair of hail stones, i and j, the total path is $R_i+r_i+r_j+R_j$ (Fig. 6). This interaction pattern may occur between any pair of hail stones, and the energy from such interactions between pairs and the ground will reach the antenna at the same time if $R_i+r_i+r_j+R_j$ is the same. Obviously the true beam path length differs from the one obtained when only *SS* with the hailstones is involved. If the depth d of the hail shaft satisfies $d < r_j$, where r_j is the distance between the scatterer farthest from the radar and the ground, then all scatterer pairs within the beam intersecting the shaft can produce signals that add up at the radar. In that case there would be $M(M-1)$ interactions, where M is the number of scatterers.

The geometry in Fig. 6 can be simplified. In Fig. 7 the range from the radar to the center of the common scattering volume (i.e. the intersection of the beam with the shaft) is denoted by R. The cone with the vertex at the center of the shaft is intersecting the ground at the distance r. Following the notation introduced in Section 2 the radar equation (7) for the three body scattering has the following form [22]:

$$P_R^{3-body} = \frac{P_T G_0^2 \lambda^2 \pi \theta_d^2 (c\tau/2)}{(4\pi)^3 (R+r)^2 8\ln(2)} \frac{\pi \theta_d^2 (R+r)^2 d^2 \sigma(\theta_r) \oint [N(D) I(\theta,\varphi)\, dD]^2 ds}{16\ln(2)\pi^2 r^4 \cos\theta_r} \tag{12}$$

The backscattering cross-section per unit area of the ground is $\sigma(\theta_r)$. This is an average value for grazing angles θ_r, and it is assumed to be the same everywhere at the intersection of the cone with the ground. Its usual units are m^2 per m^2 and is often given in dB [29]. $I(\theta,\varphi)$ is the power flow due to scattering in the usual directions, and $ds = r\cos\theta_r\, d\psi$ is the line element along the circle (base of the cone). The main approximation is that the center of the common (scattering volume) is representative for all scatterers, hence distances and angle are referenced to its location. This is why the integration is along the circle on the ground as opposed to ellipses. Note that the returned power P_r is twice the one reported in [22] who did not account for coherent summation due to bidirectional propagation within each pair of scatterers. The first fraction in (12) contains all the terms of the weather radar equation except the reflectivity factor Z_s of the three body scattering signature at range $(R+r)$. It is given by the second fraction as (corrected equation (9) in [22])

$$Z_s^{3-body} = \frac{\lambda^4}{\pi^5 |K_w|^2} \frac{\pi \theta_d^2 (R+r)^2 d^2 \sigma(\theta_r) \oint [N(D) I(\theta,\varphi)\, dD]^2 ds}{32\ln(2)\pi^2 r^4 \cos\theta_r}. \tag{13}$$

The expression from Eq. (12)

$$\frac{\sigma(\theta_r) \oint [N(D) I(\theta,\varphi)\, dD]^2 ds}{4\pi r \cos\theta_r} = \frac{\sigma(\theta_r) \int_{\theta_r}^{\pi-\theta_r} [N(D) I(\theta,\varphi)\, dD]^2 d\theta}{4\pi} \tag{14}$$

characterizes the interaction between the scatterers in the atmosphere and on the ground.

3.1.2. An observation

Hail storms that occurred on March 31, 2008 in Oklahoma are briefly discussed. Several of these storms exhibited a pronounced *TBSS*. Fig. 8 illustrates the reflectivity factor on a conical surface (elevation angle = 3.1°), whereas vertical cross-sections of this event are depicted in Fig. 9. The storms had reflectivity factors up to 70 dBZ and produced hail sizes of up to 44 mm. A radial of the reflectivity factor at elevation 3.1° is illustrated in the bottom panel of Fig. 8.

The *SS* reflections along the radial end at about 124 km where the radial gradient of reflectivity is largest. Beyond it, effects of *TBSS* are evident. Within the *TBSS* the field of differential reflectivity ($Z_{DR} \equiv Z_{hh}(\mathrm{dB}Z) - Z_{vv}(\mathrm{dB}Z)$) has a pronounced maximum (>5 dB) immediately adjacent to the strong downward gradient of Z. That part of the Z_{DR} is produced by interaction of hail with ground directly below the shaft. Scattering of vertically polarized fields from hail to the ground is minimal at the scattering angle of 90° (directly below the storm) whereas scattering of the horizontally polarized fields has a broad maximum in that direction. This

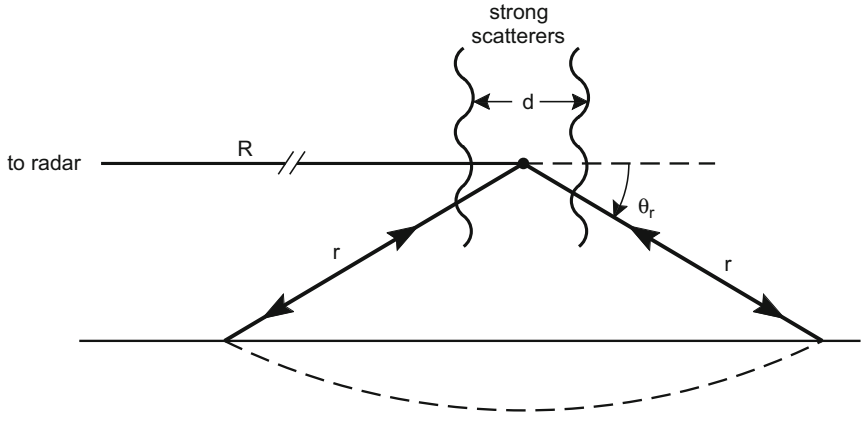

Fig. 7. Simplified representation of the geometry in the three body scattering process. The distances are with respect to the scattering center in the middle of the shaft. The beam is assumed parallel to the ground and the distance to the radar is R; r is the distance between the scattering center and the ground corresponding to the indicated forward scattering angle θ_r.

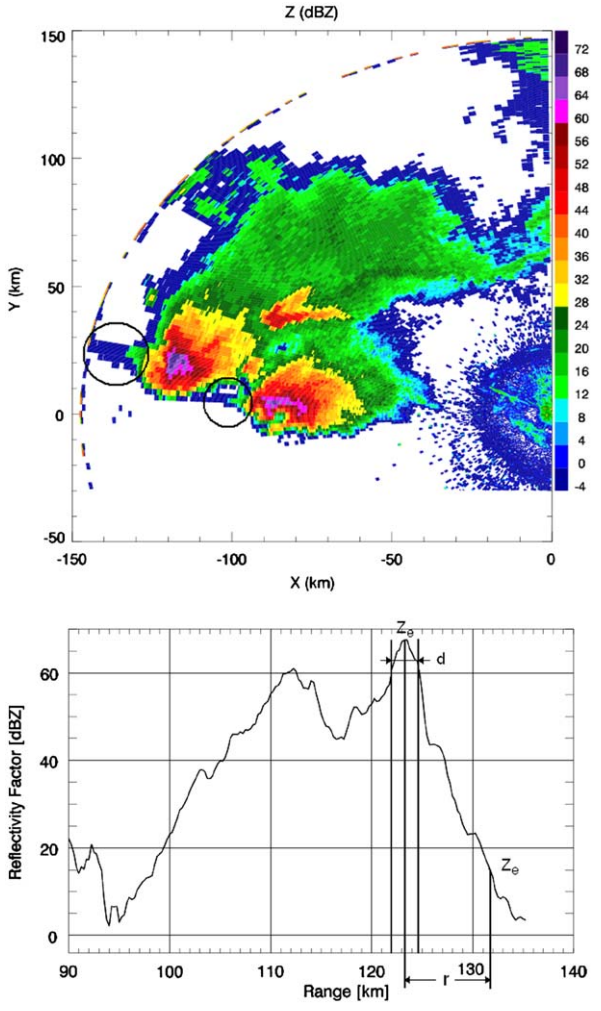

Fig. 8. Top panel: 3.1°−elevation PPI display of the reflectivity factor of the storm from March 31, 2008. The signature of the hail spike is easier to spot in the more distant storm (circled, 120 km at ~290°) than the closer one (circled, 90 km and same azimuth). Bottom panel: reflectivity factor along the radial at 282° azimuth.

combined effect has caused the observed maximum of Z_{DR}. Further in range are the returns (via *TBSS*) coming from the rings centered on the hail shaft axis and characterized by a gradual decrease in Z_{DR}. Due to the scattering pattern of hailstones (approximately modeled as spheres) the contribution to the vertically polarized return mediated via the ground increases while the contribution to the horizontally polarized return decreases causing the observed dependence. Note the remarkable decrease in the cross-correlation coefficient in the *TBSS*. This is expected as the triple scattering independently de-correlates the returns. Hence the correlation coefficient (bottom panel in Fig. 9) is reduced.

The peak reflectivity, the width of the hail shaft d, and the distance to the ground r are indicated in the bottom panel Fig. 8. In this case we obtained d from the width of the reflectivity profile between the points—6 dB below the peak. This is consistent with the accepted definition of the range resolution volume [1]. The reasons *TBSS* s are not observed more often could be in the weak values below display thresholds or in obscuration by stronger precipitation echoes.

3.2. Mirror images

Mirror-images refer to reflectivities measured by air- or space-borne radars at ranges beyond the range of the surface reflection. These reflectivities are produced by radar pulses that have been reflected off the Earth's surface, are then backscattered by precipitation, and are finally reflected off the Earth's surface a second time towards the radar receiver (Fig. 10). For nadir viewing angles the effect produces an echo exactly in the mirror position; the continuous and the dashed paths depicted in Fig. 10 are in fact equivalent in terms of time delay.

Meneghini and Atlas [30] derived a closed expression for the mirror image power return:

$$P_m(t') = \frac{C_r\,\eta_j \Gamma^4 \sigma_0}{\sigma_0 H_r^2 \theta_d^2 + 2.76 \Gamma^2 H_j^2}\, 10^{-0.2(\mathcal{A}_T + \mathcal{A}_j)} \tag{15}$$

where C_r is the radar constant, η_j the backscattered rain reflectivity factor, σ_0 the normalized backscattering cross-section of the surface, H_r the height of the radar, θ_d the 3-dB beamwidth, Γ^2 the Fresnel reflectivity of the surface, $\mathcal{A}_T$ the path-integrated attenuation (in dB) from storm top to surface, and $\mathcal{A}_j$ the path-integrated attenuation from surface to H_j. Eq. (15) is valid under the assumptions that the medium is approximately isotropically scattering, the surface can be treated in the scalar Kirchoff approximation and the altitude of the radar is much larger than its footprint radius at the surface. This model has been extended by [31] to include polarization and the so-called bistatic component [i.e. the contribution from radiation scattered by the precipitation/surface to the surface/precipitation and then back to the radar (see red dashed lines in Fig. 10), which typically contributes to the radar return within the first kilometer below the surface]. Besides the precipitation reflectivity itself (η_j), the mirror echo power is affected by the scattering properties of the surface (σ_0, Γ^2), by the path attenuation properties of the scene ($\mathcal{A}$) and by the geometry of illumination (H_j and H_r). The ratio of the mirror (P_m) to the direct (P_d) echo power derived from Eq. (15) by [32]

$$\frac{P_m(t')}{P_d(t)} = \frac{(H_r - H_j)^2 \Gamma^4 \sigma_0}{\sigma_0 H_r^2 + 2.76 \Gamma^2 H_j^2/\theta_d^2}\, 10^{-0.4\mathcal{A}_j} \tag{16}$$

can lead to a better insight into the rain attenuation properties, and finally to rain rate and liquid water content retrievals (e.g. [31, Section V]). The mirror returned power is generally lower than the direct returned power as roughly depicted in the right side of Fig. 10 (see also [32, Fig. 2]), with the correlation between mirror to the direct echo power being stronger when nadir observations are considered [32, Fig. 7].

Meneghini and Atlas [30], Liao, Meneghini and Iguchi [31], Li and Nakamura [32,33] studied the range of rain rates over which the mirror image is detectable in the Tropical Rainfall Measuring Mission (TRMM) and GPM space-borne configurations. In TRMM data the 13.5 GHz radar can detect the mirror image clearly over the ocean; most of the mirror return power over land seems much

Please cite this article as: Battaglia A, et al. Multiple-scattering in radar systems: A review. JQSRT (2010), doi:10.1016/j.jqsrt.2009.11.024

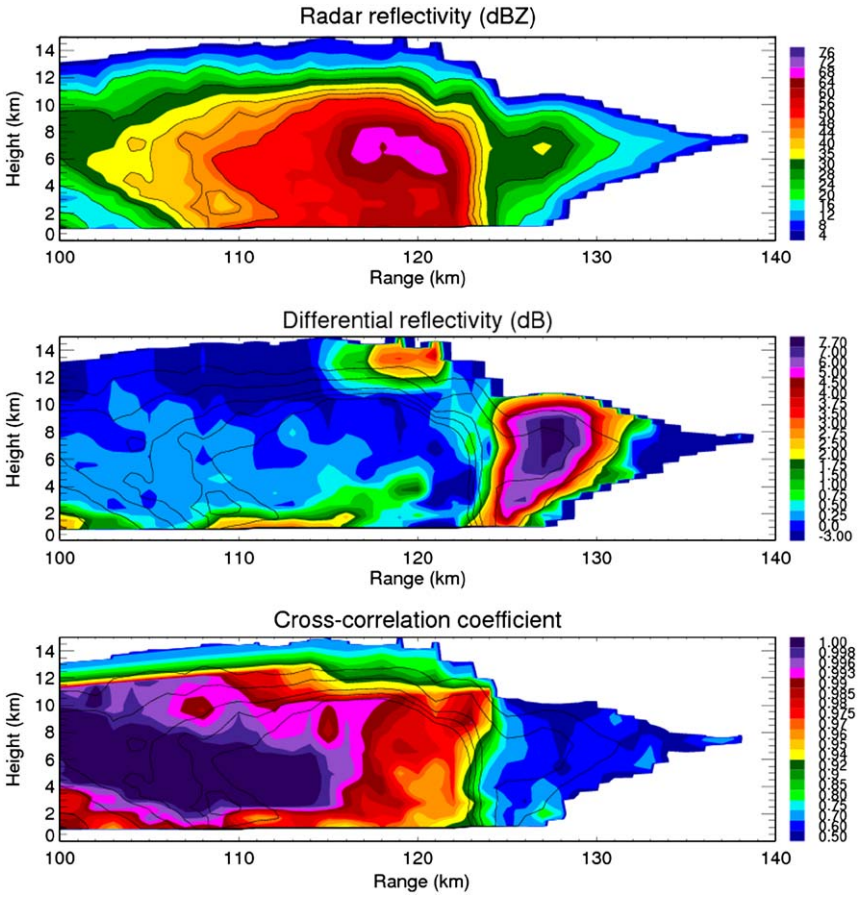

Fig. 9. Vertical cross-sections of equivalent reflectivity factor at horizontal polarization Z_{hh}, differential reflectivity Z_{DR}, and cross-correlation coefficient from the same volume scan as in Fig. 8.

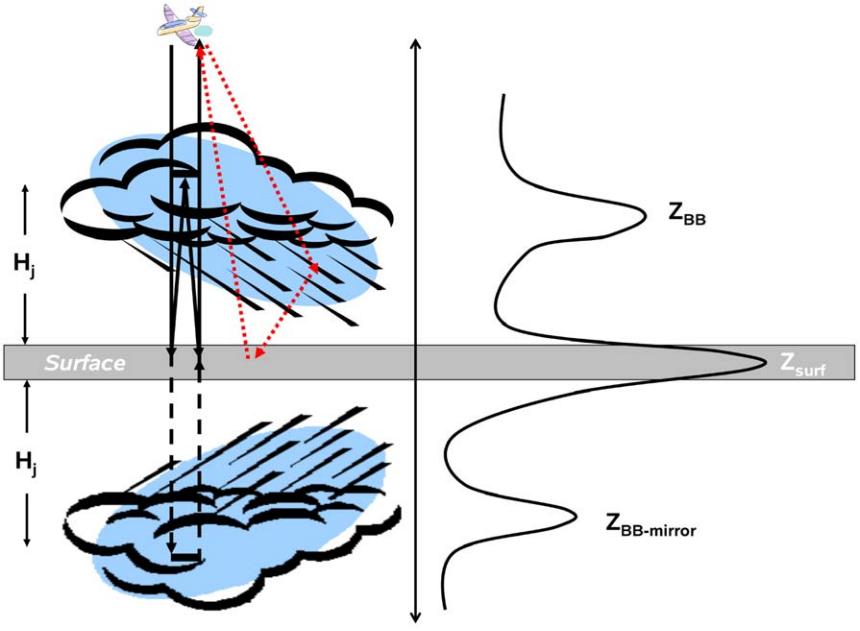

Fig. 10. Schematic presentation of the mirror image echo. H_j is the height of the mirrored region. By way of example a bright band peak Z_{BB} with its mirror image is depicted. The red dashed lines represent the bistatic scattering contribution. (For interpretation of the references to color in this figure legend, the reader is referred to the web version of this article.)

Please cite this article as: Battaglia A, et al. Multiple-scattering in radar systems: A review. JQSRT (2010), doi:10.1016/j.jqsrt.2009.11.024

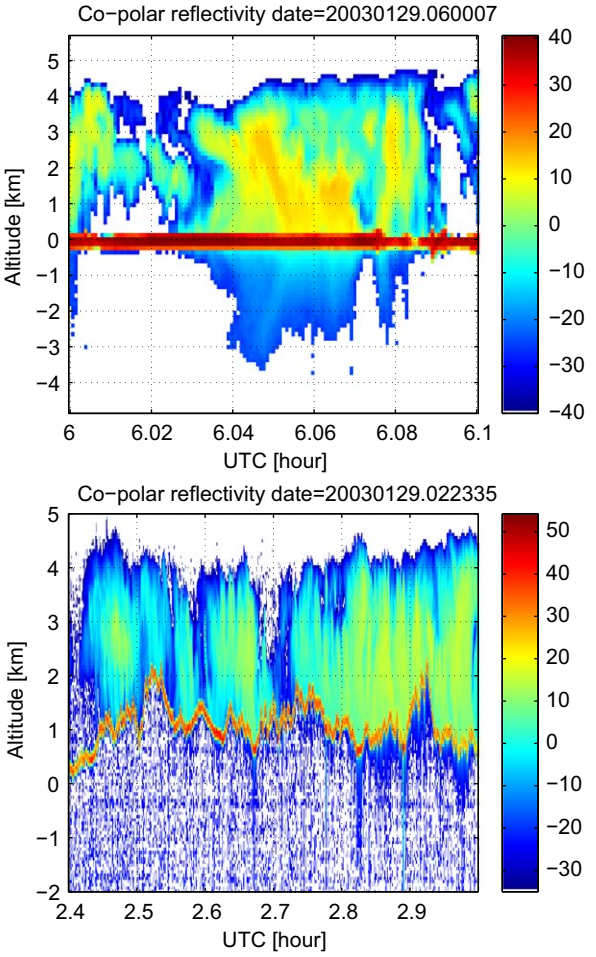

Fig. 11. Reflectivity profiles collected by the Airborne Cloud Radar (ACR) nadir-looking 94 GHz cloud radar [100] on-board the NASA P-3 flying at about 6 km altitude during the Wakasa Bay field campaign with a clear example of mirror image (top panel) and the absence of it (bottom panel). The top (bottom) image corresponds to a flight over the ocean (the mountainous region close to the coast).

lower than that over ocean (due to the lower Fresnel reflectivity of land surfaces). This is confirmed also in Fig. 11 where the presence of the mirror image can be noticed above sea (top panel) but not above a jagged mountain (bottom panel). Li and Nakamura [32] observed, for the same direct image echo intensity, larger variability of the mirror image echo over land than over ocean. Above mountain regions the rain mirror echo can be severely contaminated by the surface return over several kilometers below the surface.

The mirror image characteristics of the TRMM precipitation radar were investigated to estimate the radiative extinction associated with melting precipitation in stratiform rain areas [34] as well.

4. Techniques to compute MS in radar systems

Simulating the *MS* produced in radar systems poses new challenges. First, a correct simulation of the signal has to account for the radar antenna pattern because the detection of *MS* waves is especially dependent on catching photons off the exact antenna axis. Therefore a full 3D spread of radar signals has to be produced, which largely increases the computational demands. Second, polarization properties (e.g. horizontal or circular polarization) need to be taken into account, because this—as will be seen later—exhibits characteristic effects on polarization diversity Third, wide-angle side scattering (*MS* regime II) is the main mechanism for *MS* in radar system, similarly to wide field-of-view lidar applications. This necessitates to take 3D structures of the clouds and the surface into account, thus 3D codes are mandatory to evaluate this effect. While analytical approximations limited to narrow-angle scattering (scattering regime I) have been developed to simulate narrow field-of-view lidar signals (e.g. [10,35,13]) not as much effort has been devoted to wide field-of-view applications. Recognizing this new challenge, the Intercomparison of 3D Radiation Codes (e.g. [36–38], and visit http://i3rc.gsfc.nasa.gov/I3RC-intro.html) has included some tests for evaluating radiation models that simulate wide field-of-view lidar/radar signals in thick clouds.

Hereafter we briefly describe available techniques for treating this thorny problem. We can distinguish between two categories of studies addressing radar *MS* simulations.

- The *time-independent analytical wave* (*vector*) *theory* (Greens function method, see [39, Chapter 4]) accounts for the so-called backscattering enhancement (e.g. [40–42]). This technique is best suited for "continuous wave radar" modeling (i.e. stationary processes), while it is of limited use for pulsed radar systems as discussed in Appendix A3 by [40].
- The time-dependent (vector) radiative transfer equation considers only the incoherent backscattering power, i.e. the backscattering enhancement is inherently ignored (e.g. [43–49,19,20]). This techniques is useful for "short-pulsed radar" modeling.

For both theories modeling has evolved in the last decade from pure scalar plane wave theories to the inclusion of antenna patterns and polarization.

4.1. Time-independent analytical wave theory and backscattering enhancement

The time-independent theory of *MS* does not accurately give the reflectivity of a pulsed radar as a function of range. However, it gives the theoretical upper limit of *MS*. Furthermore, it can give a rough estimation of reflectivity of a pulsed radar in some conditions as described in Appendix of [40]. By the same token, this theory cannot be applied directly to atmospheric continuous wave radars, since they are generally implemented with frequency modulation to achieve range resolution in the frequency domain (instead of time domain as in pulsed radars) and the resulting variation of the carrier frequency with time is not captured by this theory. The

Please cite this article as: Battaglia A, et al. Multiple-scattering in radar systems: A review. JQSRT (2010), doi:10.1016/j.jqsrt.2009.11.024

same is true for other continuous wave radar systems achieving range resolution by other means (e.g. phase coding). In practice, the theory could be more directly applied to telecommunication links and the derived atmospheric applications based on path integral attenuation, once a bistatic formulation is adopted.

Unlike the time-independent radiative transfer theory, the time-independent analytical wave theory calculates scattered intensity directly from amplitude and phase. A pioneering work of [50] theoretically predicted that the scattered signal in a random medium will be enhanced by the contributions of time reversal-light-paths near right backscattering angles. This prediction was experimentally demonstrated by [51]. The underlying idea is depicted in Fig. 12, where two terms are schematically depicted. In Fig. 12a, two incident waves E_A and E_B satisfy the right backscattering condition (i.e. the angle between incident and scattered direction is exactly 180°). The measured intensity is given by two terms: the incoherent intensity (self-conjugation) represented as $|E_A|^2$ or $|E_B|^2$, referred to as ladder term, and the term given by the time-reversal conjugation: $Re(E_A \cdot E_B^*)$ or $Re(E_B \cdot E_A^*)$, referred to as cross-term. As long as the right backscattering condition is satisfied, the phase factors of E_A and E_B in the cross-term cancel out, giving a finite contribution when summing up the time-reversal conjugations from the particles in the random medium. On the other hand, if the right backscattering condition is not satisfied as shown in Fig. 12b, the phase factor remains in $Re(E_A \cdot E_B^*)$, giving a strong de-correlation when the addition is performed over many particles, and the resulting inhibition of the backscattering enhancement.

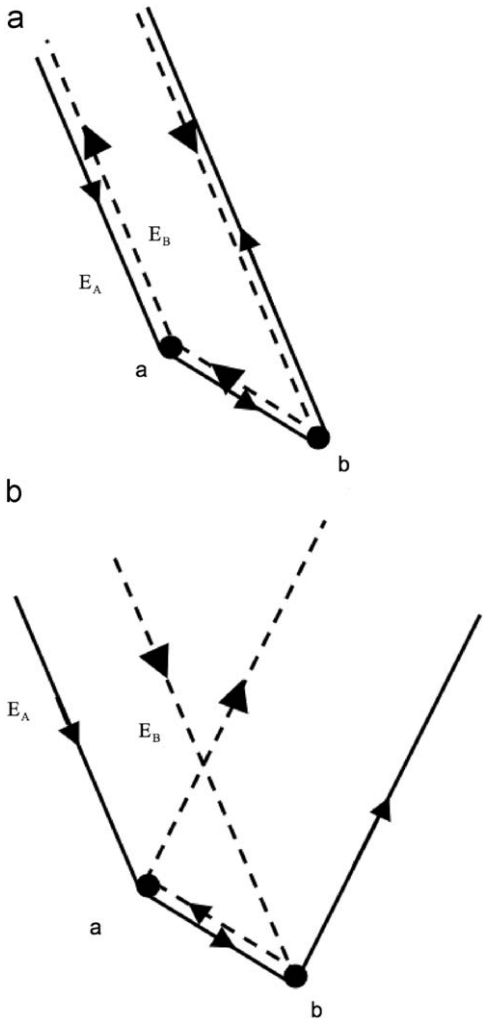

Fig. 12. Double scattering in (a) a perfect backscattering condition and (b) in non-exact backscattering. Extracted from [48].

Further intensive works from 1970s to early 1990s concentrated physical–mathematical works of these two terms (see reviews by [52,53]). Before 2000s the theoretical studies of backscattering enhancements considered only the plane wave incidence and its scattered wave was assumed to be received at infinite range. Speaking of the scalar wave theory of the plane wave incidence, up to that time, a general analytical solution of both ladder and cross-terms for isotropic scattering media [54], and for anisotropic scattering media were derived [55]. Perhaps, due to this historical reason, there was a controversy whereby some researchers thought that the backscattering enhancement would occur only for the plane wave incidence, or it would be negligible within a narrow angular cone centered about the right backscattering direction. As a consequence, research in this field was revitalized only in 2000s thanks to successful operations of millimeter-wavelength radars.

Kobayashi et al. [56,40] expanded a vector analytical wave theory, originally derived as a plane wave theory by [57], to a spherical wave theory by assuming Gaussian transmitting and receiving radiation patterns in the regime of the second order scattering. Spherical water particles of a uniform size were assumed to be randomly distributed with a finite thickness d in an infinitely extended layer. The second order ladder term for the finite beam width is derived as (details in [40])

$$
\begin{aligned}
I_L^{[2]} = {} & P_T G_0^2 \lambda^2 \theta_d^2 (2^7 \pi \ln 2\, r^2)^{-1} N_0^2 \{2(\kappa''_{iz} + \kappa''_{sz})\}^{-1} \\
& \times \int_0^\infty d\eta \int_0^{2\pi} d\phi \int_0^d d\zeta \frac{\eta}{1+\eta^2} \exp[-k_{ext}\sqrt{1+\eta^2}\,\zeta] \\
& \times \exp[-\zeta^2\eta^2/4\sigma_r^2] \sum_{\hat{\alpha}} \{|\langle \hat{\alpha}|F(\hat{k}_s, \hat{r})\, F(\hat{r}, \hat{k}_i)|\psi_0\rangle|^2 \\
& \times [\exp\{-2\kappa''_{iz}\,\zeta\} - \exp\{2\kappa''_{sz}\,\zeta - 2(\kappa''_{iz} + \kappa''_{sz})\,d\}] \\
& + |\langle \hat{\alpha}|F(\hat{k}_s, -\hat{r})\, F(-\hat{r}, \hat{k}_i)|\psi_0\rangle|^2 [\exp\{-2\kappa''_{sz}\,\zeta\} \\
& - \exp\{2\kappa''_{iz}\,\zeta - 2(\kappa''_{iz} + \kappa''_{sz})\,d\}]\}
\end{aligned}
\tag{17}
$$

where σ_r is the 3-dB footprint radius, $\hat{k}_i$ and $\hat{k}_s$ are the incident and scattered directions, $F(\hat{k}_s, \hat{k}_i)$ denotes the scattering amplitude matrix scattered from the directions $\hat{k}_i$ to $\hat{k}_s$, κ''_{iz} and κ''_{sz} are the extinction rate in the directions of incident and scattered angles, N_0 is the particle number density, ψ_0 represents the initial polarization state and $\hat{\alpha}$ is the polarization (H or V), $\eta \equiv \tan\theta$, φ and ζ are integral variables with φ and θ the polar angles in spherical coordinates. The second order cross-term for the finite beam width can be derived in a similar manner

to the second order ladder term. The result is

$$I_C^{[2]} = P_T G_0^2 \lambda^2 \theta_d^2 (2^7 \pi \ln 2\, r^2)^{-1} N_0^2 \,(\kappa''_{iz} + \kappa''_{sz})^{-1} \times \int_0^{\infty} d\eta \int_0^{2\pi} d\phi \int_0^{d} d\zeta \frac{\eta}{1+\eta^2} \exp[-\{k_{ext}\sqrt{1+\eta^2} + \kappa''_{iz} + \kappa''_{sz}\}\zeta] \exp[-\zeta^2\eta^2/4\sigma_r^2]\{1 - exp[-2(\kappa''_{iz} + \kappa''_{sz})(d-\zeta)]\} \times Re\left[\left\{\sum_{\hat{\alpha}} \langle \hat{\alpha}|F(\hat{k}_s, \hat{r})\, F(\hat{r}, \hat{k}_i)|\psi_0\rangle^* \langle \hat{\alpha}|F(\hat{k}_s, -\hat{r}) \times F(-\hat{r}, \hat{k}_i)|\psi_0\rangle\right\} \exp[i(k_{dz} + t)\zeta]\right] \quad (18)$$

in which the deviation vector $\mathbf{k_d}$ from the backscattering direction and the new variable t are defined as

$$\mathbf{k_d} = k(\hat{k}_s + \hat{k}_i) \equiv k_{dx}\hat{x} + k_{dy}\hat{y} + k_{dz}\hat{z} \quad (19)$$

$$t \equiv k_{dx}\eta \cos\varphi + k_{dy}\eta \sin\varphi. \quad (20)$$

The derived formulas of the cross-terms reduce to those of the plane wave theory in the limit of a large footprint size, which means that the backscattering enhancement exists even for the spherical wave that is transmitted and received by an antenna of a finite beam aperture angle. Furthermore the intensities of the cross-terms as well as those of the ladder terms strongly reduce, when the footprint radius is smaller than the mean free path in a random medium. This reduction becomes more significant as the optical thickness of the medium increases. In their calculation, the backscattering enhancement for the finite beam width is crucial within a bistatic scattering angle λk_{ext}, which was also shown as a general characteristic of the plane wave theory [54,58].

Ihara et al. [59] experimentally studied backscattering enhancement under a finite beam width. In their experiment, a 30 GHz radar with a 3-dB beam width of 10° was used, and water-filled spheres of polystyrene were randomly placed in a polystyrene foam. To precisely control small scattering angles, they developed a mirror image technique. Their measurement clearly showed backscattering enhancement in both co- and cross-polarized returns with roughly twice the intensity of the far-backscattering angles. The far-backscattering angle can be defined as the region beyond a deviation angle of 5 times λk_{ext} from the right backscattering angle. For instance, in the case of 95 GHz within a medium with $k_{ext} = 10\,\mathrm{km}^{-1}$ it corresponds to the region beyond a deviation angle of 0.01°. The width of bi-static enhancement scattering angles of the cross-polarized return is smaller than that of copolarized one as expected from the theory [57,40]. In principle this theory can be extended to obtain the relation of the ladder and cross-terms to the footprint size.

In studies of the radiative transfer equation, the direct products of electromagnetic fields have been often used for the sake of mathematical simplicity (e.g. [60]). Mishchenko [61] adopted this technique to study general characteristics of backscattering enhancement factors. His conclusion is that a cross-term is not always equal to the corresponding ladder term, which was earlier reported by [62] through vector-based scattering simulation. These problems were also scrutinized in the 2000s by [42,41], and both were at the same time concerned with the backscattering enhancement under a finite beam width. Oguchi and Ihara [42] developed a computer-simulation by applying the method of [61], and taking into account a Gaussian shaped directivity/gain function of the antenna. Spherical water particles of a uniform size were assumed to be randomly distributed in a volume of finite width and thickness. They introduced a statistical technique for calculating scattering to as high as 7th order. They carefully treated *MS* paths based on Twersky's theory [63], paying special attention to "specific paths (e.g. Fig. 13d in the case of triple scattering), in which a scattered light travels the same path twice or more. In these paths, one path of a light and its time-reversal path coincide with each other, and apparently the number of the former paths overcomes the latter, resulting in the inequality of the intensities of the ladder and cross-terms. Hence, they suggested that in their simulations the contributions from these paths must be added to the cross-terms. Their results are summarized as follows. (1) In copolarized return, the backscattering enhancement curve becomes sharper with the order of scattering. (2) In cross-polarized returns, the ladder and cross-terms are equal in the second order scattering, which is exceptionally true for the case of spherical particles. An explicit proof of this assertion can be found in [40]. Nonetheless, beyond the second order, the differences between these two terms increase with the order of scattering. Actually, at the 7th order scattering, the ladder term in the cross-polarized return strongly approaches to the ladder term in the copolarized return, while the cross-term in the cross-polarized return keeps almost a constant difference from the ladder term in the

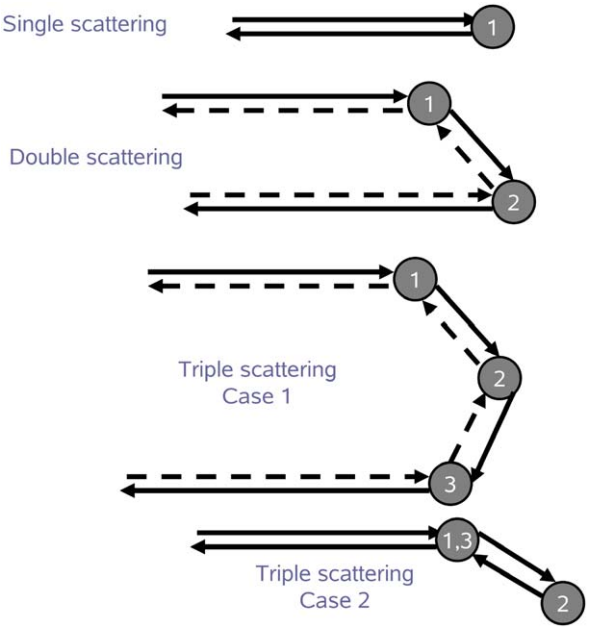

Fig. 13. Schematic diagram of the scattering process at different scattering order (adapted from [42]).

copolarized return by about 10 dB from 2nd to 7th order of scattering. In addition, the relation of the ladder and cross-terms to the footprint size, mentioned earlier in this section, were also confirmed by their calculation.

Kobayashi et al. [41] expanded their second-order analytical-wave theory to spheroidal water and ice particles of uniform size to study the backscattering enhancement under illumination by a finite beam width, particularly to evaluate the difference of the ladder and cross-terms as generally formulated by [61]. Their results for spheroidal water particles of 1 mm diameter with eccentricity $0.4 \le \varepsilon \le 1$ are:

- in copolarized return, the ladder and cross-terms are equal for any ε;
- in cross-polarized return, the ladder term is larger than the cross-term; the difference reaches 3 dB for $\varepsilon = 0.4$, whereas, as expected, there is no difference for $\varepsilon = 1.0$ (i.e. sphere).

The results for ice particles with $0.3 \le \varepsilon \le 3$ are:

- in copolarized return, the ladder and cross-terms are equal for any ε;
- in cross-polarized return, the differences of these two terms are negligible.

When [43] attributed their measured linear-depolarization-ratios (*LDR*) of high values to the *MS* effect, they adopted the sphere-particle approximation, which naturally caused skepticism because the high *LDR*'s could be attributed to the polarization effect of single scattering coming from highly canted spheroidal rain drops. Kobayashi et al. [41] considered this problem. The shape of a raindrop was approximated by a spheroid based on [64,65] with $\varepsilon = 1 - 0.05D$, where D is the diameter of an equivolumic sphere in mm. The distribution of rain drops was assumed as the Marshall–Palmer form. The thickness of a rain-layer was set at 500 m. The footprint radius of a radar was assumed to be infinite to evaluate the maximum deviation between the spherical and spheroidal approximations. Under these assumptions, a variety of canting angles have been considered. Even at the rain rate of 15 mm/hr, the maximum difference in these two approximations is negligible. Hence, the adoption of the spherical approximation to rains is legitimated. When an extremely high canting angle of 45° is assumed, the intensity of the first order scattering (I_1^{cx}) in the cross-polarized return is smaller than that of the second order one (I_2^{cx}), by 10 and 20 dB at 35 and 95 GHz, respectively, for the infinite footprint radius. By comparing Figs. 14 and 15 it is noted that when the actual footprint radius is taken into account, the value of I_1^{cx} is invariant, whereas that of I_2^{cx} reduces. However as shown in Figs. 14a and 15a, the value of I_2^{cx} is almost invariant near its maximum (about −45 dB) regardless of the footprint radius. When the finite footprint effect is taken into account, the value of I_2^{cx} is reduced by about 1–2 dB in comparison with the infinite footprint case; however, the former never becomes smaller than I_1^{cx} even though considering strongly deformed and canting rain drops. As a conclusion, at millimeter wavelength frequencies, cross-polarized returns from rain drops are dominated by *MS*.

There is another issue that will be important for the spaceborne monostatic radar compared to the air-borne/ground-based monostatic radar, because the former radar should be approximated by a bistatic radar with a bistatic angle of about 0.001°. Computer simulations by [62,66], indicated that, if vector-based scatterers are considered, the intensities of cross-terms (backscattering enhancements) in copolarized return signal are equal between parallel and orthogonal angular displacements only in the case of the exact backscattering angle, whereas these two cross-terms have different values in the case of not-exact backscattering angles. On the other hand, in the cross-polarized return, these two terms are always equal between the two angular displacements. These

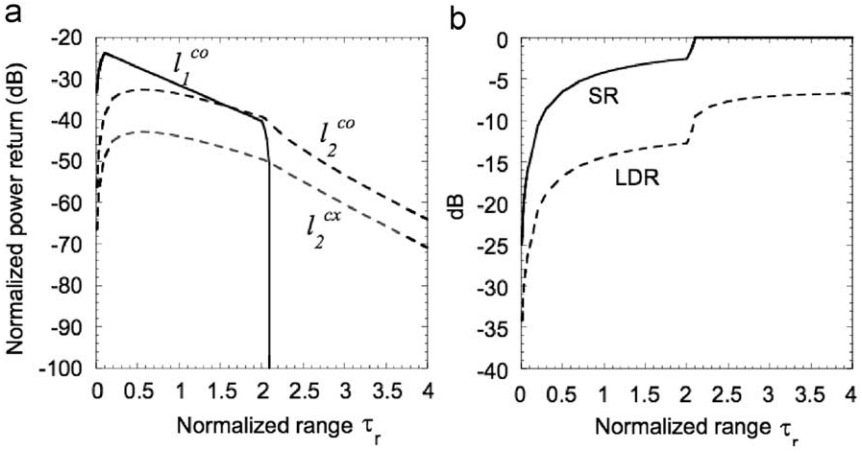

Fig. 14. (a) The normalized power-returns I_1^{co}, I_2^{co} and I_2^{cx} plotted as functions of the normalized range τ_r (see Section 4.3.1 for notation). Note that I_1^{co} vanishes after $\tau_r = 2.1$. (b) The ratio $I_2^{co}/(I_1^{co}+I_2^{co})$ (*SR*) and the linear depolarization ratio (*LDR*) versus τ_r both expressed in dB. A layer of spherical water particles of uniform diameter $D = 1$ mm has the optical thickness $\tau = 2$. A pulse of the normalized range resolution $\tau_p = 0.1$ is incident on the top surface of the medium at time $t = 0$ in the beam of the normalized footprint radius $\Xi_r = 1$. The carrier frequency is set at 95 GHz. Extracted from [48].

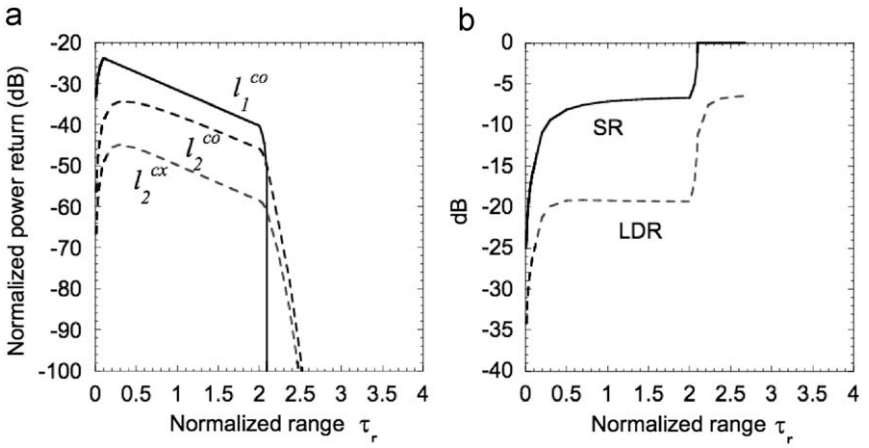

Fig. 15. Same as Fig. 14 with a smaller normalized footprint radius $\Xi_r = 0.2$.

phenomena cannot be expected for the ladder terms (radiative transfer equation). The second order theory in [40] confirmed these phenomena, and gave mathematical proofs. Oguchi and Ihara [42] also confirmed these spatial anisotropies of the cross-terms via simulation. It is thus summarized that when the backscattering enhancement is considered for the space-borne radar, it is important to determine in which direction the initial linear polarization is aligned, parallel or orthogonal to the along-track of a satellite.

4.2. Pulsed radars and time-dependent RTE

This time-dependent analytical formalism is based on the solution of the time-dependent vector radiative transfer equation. Thus Stokes parameters (intensities) rather than EM fields are simulated and as usual, the time-dependent radiative transfer equation can be phenomenologically derived. Ishimaru [67] derived it by using the two-frequency mutual coherence function [68,63]. In the same paper, he derived a time-dependent diffusion equation with an additional second-order differential term $((3/c^2)(\partial^2/\partial t^2))$, which implies that the net flux of flow of a diffuse intensity propagates at the speed of $c/\sqrt{3}$ in a very dense medium. Ito and Oguchi [69] removed this term by imposing that a necessary condition be satisfied in the diffusion approximation. This controversy still seems to be an open issue in terms of precisely controlled experiments. However, because the diffusion equations of both authors were derived from the same time-dependent radiative transfer equation, it will be no matter to start the analysis from the time-dependent radiative transfer equation.

Another issue is related to the effective wave number and absorption constant. Both have been derived from the Foldy–Twersky–Oguchi formula [55,2]. Because infinite space (no boundary), and completely randomness (no particle–particle correlation) is assumed in its derivation, [70] advise caution in applying this formula to a small volume.

4.2.1. Monte-Carlo techniques

Monte-Carlo techniques have been widely exploited to simulate lidar *MS* effects ([71] and reference therein). The Monte-Carlo approach is based on computer simulation of "photon trajectories" (actually photons are not traced but energy parcels which can be described by the Stokes parameters). The expected values of the signal is estimated by averaging over a large ensemble of independent samples. The elements of the trajectories, i.e. free-path lengths and scattering angles, are chosen from the probability distributions of the influencing physical parameters. The parameters required to characterize the scattering medium are the three-dimensional structure of the volume extinction cross-section, the *SS* albedo of the medium, and the *SS* phase matrix. "Photon trajectories" are constructed and the path of each transmitted "photon" is followed from the transmitter through *MS* events in the cloud to the receiver. To improve computational efficiency variance-reduction techniques are typically applied.

An important simulation capability recently added to 3D Monte-Carlo models is polarization. As described in [72–74], these models consider polarization by keeping track of not only the location and direction of simulated "photons" but also the fraction of horizontally and vertically polarized intensity represented by each "photon".

The same conceptual scheme developed for lidar systems was first applied to radar by [20]; they showed that in the presence of strongly attenuating media (i.e. heavy precipitation), *MS* contributions will enhance the detection of rain by partly overcompensating the apparent path attenuation. Their study, however, did not explicitly account for the antenna pattern, which overestimates the *MS* enhancement. Based on the Monte-Carlo solution of the vector radiative transfer equation [73], [46,24] developed a radar *MS* simulator, capable of treating both polarization and antenna pattern. The model was successively upgraded to include the interaction with a Kirchoff surface, which realistically reproduces the effect of water surfaces [19]. Radiation is launched from

Please cite this article as: Battaglia A, et al. Multiple-scattering in radar systems: A review. JQSRT (2010), doi:10.1016/j.jqsrt.2009.11.024

the radar with directions and polarization state resulting from the antenna pattern, and it is traced through the scattering medium by simulating all stochastic processes (e.g. distances traveled before interaction, scattering angles). A biasing technique allows the evaluation of contributions to radar reflectivity of each scattering order. The k-order of scattering contribution to the Stokes vector received by the radar for a particular photon (j) will be

$$\bar{I}_a^{(k)}(r)[j] = F_n^{rec.}(\hat{\mathbf{\Omega}}_v^{(k)}) P_{prop}(\vec{\mathbf{r}}_{scat}^{(k)} \rightarrow \vec{\mathbf{r}}_{rec.})\, S_{scat}(\vec{\mathbf{r}}_{scat}^{(k)}; \hat{\mathbf{\Omega}}_i^{(k)}, \hat{\mathbf{\Omega}}_v^{(k)}) \bar{I}(\vec{\mathbf{r}}_{scat}^{(k)}) \tag{21}$$

S_{scat} represents the normalized phase matrix for the medium at the point $\vec{\mathbf{r}}_{scat}^{(k)}$ relative to the incoming direction of the photon before the k-order scattering, $\hat{\mathbf{\Omega}}_i^{(k)}$, and to the scattered direction towards the receiving antenna, $\hat{\mathbf{\Omega}}_v^{(k)}$ (unit vector corresponding to the vector difference $\vec{\mathbf{r}}_{rec.} - \vec{\mathbf{r}}_{scat}^{(k)}$). Obviously at the first scattering order for monostatic radar $\hat{\mathbf{\Omega}}_v^{(1)} = -\hat{\mathbf{\Omega}}_i^{(1)}$. In (21) the $F_n^{rec.}(\hat{\mathbf{\Omega}}_v^{(k)})$ scalar term takes into account the antenna pattern in the receiving segment (this term suppresses all photons scattered to the radar receiver from outside the field of view). $P_{prop}(\vec{\mathbf{r}}_{scat}^{(k)} \rightarrow \vec{\mathbf{r}}_{rec.})$ is the 4×4 propagation matrix that accounts for the extinction of the signal scattered back to the radar receiver. The apparent intensity is attributed to an apparent range which is computed by adding the total distance traveled by the photon from the transmitting antenna to the interaction point and the distance between the interaction point and the receiver antenna divided by two:

$$r^{(k)} = 0.5[dist(\vec{\mathbf{r}}_{tr.} \rightarrow \vec{\mathbf{r}}_{scat}^{(k)}) + |\vec{\mathbf{r}}_{rec.} - \vec{\mathbf{r}}_{scat}^{(k)}|].$$

By summing up over N_T photons and over the different orders of scattering the algorithm provides an estimate of the mean apparent intensity received by the radar from range r as

$$\langle \bar{I}_a(r) \rangle = \frac{1}{N_T} \sum_{j=1}^{N_T} \sum_{k=1}^{N_s} \bar{I}_a^{(k)}(r)[j] \equiv \sum_{k=1}^{N_s} \bar{I}_a^{(k)}(r) \tag{22}$$

with N_s being the maximum scattering order. When using $N_s = 1$ only *SS* effects are taken into account. This term introduced in Eq. (11) leads to the copolar (*co*) and cross-polar (*cxo*) reflectivity Z and to the linear depolarization ratio *LDR*:

$$Z_{co} = \sum_{j=1}^{\infty} Z_{co}^{[j]}, \quad Z_{cx} = \sum_{j=1}^{\infty} Z_{cx}^{[j]}, \quad LDR \equiv \frac{Z_{cx}}{Z_{co}}. \tag{23}$$

The time-dependence is accounted for by sorting radiation according to travel times. A rectangular pulse is assumed. The model accounts for arbitrary radar configurations like airborne, space-borne or ground-based, and monostatic or bistatic. Like all Monte-Carlo schemes, it is very flexible in terms of geometry and definition of scattering medium properties, but it requires large computational times to achieve high accuracies. This becomes particularly problematic if dealing with very thick media.

Although by its nature the radiative transfer equation ignores coherent effects, the backscattering enhancement can be accounted for in part by a simple way in allowing for a doubling of the copolar terms for scattering orders higher than one [70, Chapter 14], which can be easily performed for all solution methods which keep track of the contributions of different order of scattering like in the Monte-Carlo approach. This approach will overestimate the actual *MS* enhancement for moving antennas which displace the return radiation from the exact backscattering direction. This can have an effect especially for satellite-borne radars. A critical discussion about backscattering enhancement in space-borne configurations is provided in Section 2.c of [75].

A Monte-Carlo technique has also been adopted to build a look-up table database for the operational CloudSat rainfall retrieval algorithm (see [76]).

4.3. Approximation techniques

Compared to Monte-Carlo simulations analytic approximation methods can drastically reduce computational time. Faster calculations allow simulations of larger number and more optically thick scenes, and can even accommodate iterative retrievals in which retrieved parameters are adjusted using on-the-fly radiative calculations. Such approaches open the possibility for retrievals based on inverse or adjoint radiative transfer calculations.

4.3.1. Analytical solutions of the time-dependent vector radiative transfer equation

Pulse propagation problems in random media were studied, first, for the scalar wave, by using two-frequency mutual coherence functions [77,68,67]. In 1990s, development of the vector theory started.

Oguchi [60] showed that the 4×4 scattering matrix of a spheroidal particle can be separated to azimuthal and polar angle parts by the use of generalized spherical functions. Using this expansion in the two-frequency vector radiative transfer equation, [78] numerically solved a general *MS* solution for a sequence of plane-wave pulses. Thereafter, [69] derived an analytical solution of the second order scattering for a single pulse through the time-dependent vector radiative transfer equation. In both works, semi-infinite slabs of spherical water particles of a uniform size were assumed. Ito et al. [43] added the condition of a finite thickness to the random medium, and derived a second order solution. Time-trends of *LDR* derived from this solution were compared to *LDR* data measured by a 34.5 GHz radar, becoming an experimental demonstration of *MS* in heavy rains.

The time-dependent vector radiative transfer equation was expanded to beam wave (spherical wave) by [47]. Their final form is an exact integral equation. By solving this equation iteratively, the accuracy of the solution can be increased as much as desired. Theoretically, an arbitrary beam shape can be chosen in their equation. Particularly, their form is advantageous to study the reflection/transmission signal from multiply layered random medium.

Please cite this article as: Battaglia A, et al. Multiple-scattering in radar systems: A review. JQSRT (2010), doi:10.1016/j.jqsrt.2009.11.024

Kobayashi et al. [48] applied the method of [47] to a Gaussian directivity/gain function. It is noted that the radar equation can be derived as a first order solution in their formalism. To compare their results of time-independent study with those of [40], they solved up to the second order scattering for a single layered medium filled with spherical particles of a uniform diameter (1 mm). The same scenario was used in the validation study by [75]. In the case of the infinite footprint radius (plane-wave incidence and received at the infinite distance), the first order scattering I_1^{co} in copolarized return, and the second order scattering intensity in copolarized (I_2^{co}) and cross-polarized (I_2^{cx}) returns are plotted in Fig. 14a as functions of the normalized range $\tau_r = ct/2l$, where t is a returning time from the top surface of the layer and l is the mean-free-path of the medium. In the calculation, the normalized total thickness of the medium (optical thickness) is assumed as $\tau = 2$, and the pulse duration T_p is set so as to satisfy a normalized pulse duration $\tau_p \equiv cT_p/2l = 0.1$. In Fig. 14b, the ratios $SR \equiv I_2^{co}/(I_1^{co}+I_2^{co})$ and $LDR \equiv I_2^{cx}/(I_1^{co}+I_2^{co})$ are plotted as functions of τ_r. To consider the effect of footprint radius, the normalized footprint radius is defined as $\Xi_r \equiv \sigma_r/l$ for a footprint radius σ_r. In Fig. 15, a smaller footprint radius $\Xi_r = 0.2$ is used. It is noted that I_1^{co} is invariant between Figs. 14a and 15a, whereas I_2^{co} and I_2^{cx} in Fig. 15a decay faster than those in Fig. 14a. This is because the lateral scattering cannot be effectively captured when the footprint radius is much smaller than the mean free path (i.e. $\Xi_r \ll 1$). As long as the second order scattering is concerned, the asymptotic values of *SR* and *LDR* can be rigorously given as 0 and -6.4 dB, respectively, for the Mie scattering from water particles of diameter of 1 mm, whereas values of 0 and -4.8 dB (1/3) apply for the Rayleigh scattering from particles of arbitrary material and diameter. These characteristics can be used to check the accuracy of any computer simulation of *MS*.

The conclusions are summarized as follows.

1. The *MS* return increases in both polarization with the normalized footprint radius Ξ_r.
2. The effect of the footprint radius becomes more significant, as the normalized range τ_r and pulse-duration τ_p increase. This effect is more conspicuous in cross-polarized return than on copolarized one.

4.3.2. Methods based on the two-stream and diffusion approximations

In this section we outline two related methods that have been proposed to estimate the multiply scattered contribution to the measured radar or lidar return. Hogan and Battaglia [49] proposed the *time-dependent two-stream* (TDTS) approximation, in which the atmosphere varies only in the direction r at which the instrument is pointing (typically upward or downward), and assume homogeneities in the other two orthogonal dimensions. The diffuse radiation field is described by the outgoing and incoming "streams", I^+ and I^-, whose evolution with time t is given by

$$\frac{1}{c}\frac{\partial I^+}{\partial t} = -\mu_1\frac{\partial I^+}{\partial r} - \mu_1 k_{ext}(\gamma_1 I^+ - \gamma_2 I^-) + S^+ \tag{24}$$

$$\frac{1}{c}\frac{\partial I^-}{\partial t} = +\mu_1\frac{\partial I^-}{\partial r} - \mu_1 k_{ext}(\gamma_1 I^- - \gamma_2 I^+) + S^- \tag{25}$$

where the cosine of the angle between these streams and the outgoing direction is $\pm\mu_1$. The coefficients γ_1 a nd γ_2 are given by $\gamma_1 = [1-\tilde{\omega}(1+g)/2]/\mu_1$ and $\gamma_2 = \tilde{\omega}(1-g)/(2\mu_1)$.

Eqs. (24) and (25) are simply the standard time-independent two-stream equations used in climate and weather forecast models (e.g. [79–81]), but with the time derivative reintroduced from the original radiative transfer equation [82]. The three terms on the right-hand-side represent, respectively, the transport of radiation from further upstream, exchange of radiation between streams due to scattering (and loss by absorption), and a source term due to scattering from the direct unscattered beam originating from the radar. Treating the transmitted pulse as instantaneous, this source term is given by

$$S^{\pm}(r,t) = \tilde{\omega} k_{ext} \mathcal{T} \delta(t - r/c)(1 \pm 3g\mu_1)/2, \tag{26}$$

where $\mathcal{T}(r)$ is the transmission between the radar and the range r, and $\delta(t-r/c)$ is the Dirac delta function. Large particles tend to scatter preferentially forward, which is represented by $g > 0$, and from (26) this results in a greater fraction of radiation entering the outgoing than the incoming stream.

The streams $I^{\pm}$ have the units s^{-1}, since they represent the flux of radiation (in Watts) normalized by the energy of the transmitted pulse (in Joules). Hence $I^{\pm}$ contain no information about the lateral spreading of the radiation, which is needed to calculate the fraction of what is scattered back to the receiver that will lie within its field-of-view. Hogan and Battaglia [49] solved this problem by considering the energy-weighted variances of the outgoing and incoming streams, $J^+ = I^+\overline{s^2}^+_w$ and $J^- = I^-\overline{s^2}^-_w$, where $\overline{s^2}^{\pm}_w$ is the variance of the lateral distance of the radiation from the main axis of the radar or lidar beam. The evolution of these quantities may be described by integrating an additional pair of equations:

$$\frac{1}{c}\frac{\partial J^+}{\partial t} = -\mu_1\frac{\partial J^+}{\partial r} - \mu_1 k_{ext}(\gamma_1 J^+ - \gamma_2 J^-) + S^+\overline{s^2}_d + I^+\left.\frac{\partial \overline{s^2}^+_w}{\partial t}\right|_{\text{diff}} \tag{27}$$

$$\frac{1}{c}\frac{\partial J^-}{\partial t} = -\mu_1\frac{\partial J^-}{\partial r} - \mu_1 k_{ext}(\gamma_1 J^- - \gamma_2 J^+) + S^-\overline{s^2}_d + I^-\left.\frac{\partial \overline{s^2}^-_w}{\partial t}\right|_{\text{diff}} \tag{28}$$

These have exactly the same form as (24) and (25), except that the source term also includes the lateral variance of the direct outgoing beam, $\overline{s^2}_d$, and an additional term is included at the end representing a source of variance due to the expansion of the initial pulse with time (the subscript "diff" indicates that this is a diffusion-like process).

Fig. 16a shows that this method performs very well compared to Monte-Carlo calculations for an idealized case

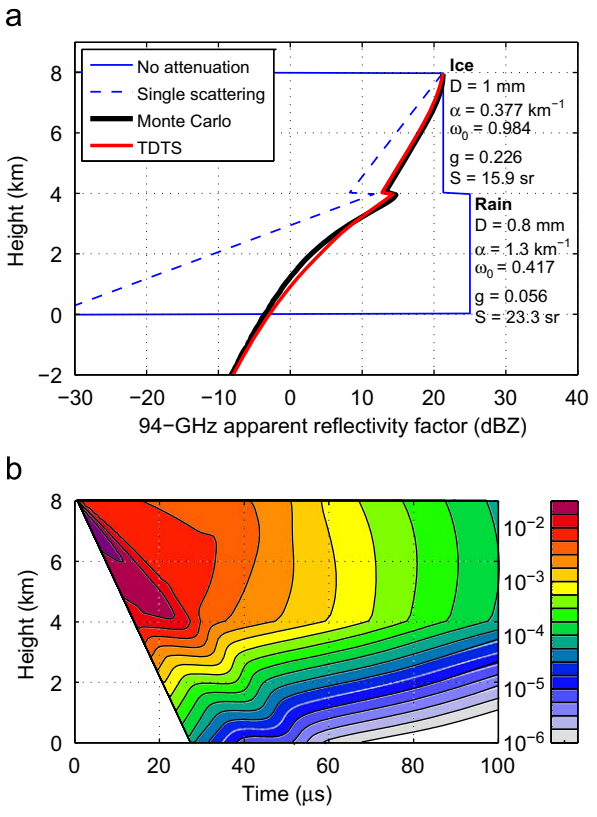

Fig. 16. (a) The apparent radar reflectivity that would be measured by the nadir-viewing CloudSat radar in a 4-km layer of ice spheres overlying a 4-km layer of raindrops, according to the [24] Monte-Carlo model and the [49] time-dependent two-stream (TDTS) method, where the size distributions are mono-disperse with diameter D, and S is the extinction-to-backscatter ratio. (b) The scalar flux $J=I^{+}+I^{-}$ (arbitrary units) as a function of comparison of time and height, calculated using the TDTS model. Note that in this case neither method included scattering by the ground.

based on the CloudSat geometry, but is about 10^6 times faster. It is currently being incorporated into the radar simulator package of [83]. Fig. 16b shows the scalar flux $(I^{+}+I^{-})$ versus time and height. The diagonal line to the left indicates the incoming pulse of radiation. The rapid attenuation of the beam in the rain layer is due to the lower *SS* albedo compared to the cloud component aloft.

The TDTS approximation is related to the diffusion approximation that has been advocated for calculating lidar *MS* [45]. We first rewrite the TDTS equations in terms of the scalar flux (also known as the actinic flux), $J=I^{+}+I^{-}$, and the net flux away from the radar, $F=\mu_1(I^{+}-I^{-})$. This leads to

$$\frac{1}{c}\frac{\partial J}{\partial t}=-\frac{\partial F}{\partial r}-\frac{J}{l_a}+\tilde{\omega}k_{ext}\mathcal{T}\delta(t-r/c) \tag{29}$$

$$\frac{1}{c}\frac{\partial F}{\partial t}=-\mu_1^2\frac{\partial J}{\partial r}-\frac{F}{l_t}+3g\tilde{\omega}k_{ext}\mathcal{T}\mu_1^2\delta(t-r/c) \tag{30}$$

where $l_a=[k_{ext}(1-\tilde{\omega})]^{-1}$ is the mean-free-path between absorption events, and $l_t=[k_{ext}(1-\tilde{\omega}g)]^{-1}$ is the transport mean-free-path. The diffusion approximation is valid for optically thick media, in which the transport mean-free-path is small, i.e. $l_t\to 0$. Assuming also that there is no absorption ($l_a\to\infty$) and the source terms are zero, these equations reduce to $\partial J/\partial t=-c\partial F/\partial r$ (expressing conservation of energy) and $F=-\mu_1^2 l_t\partial J/\partial r$ (which is essentially Fick's law of diffusion). Substitution of one into the other yields the familiar diffusion equation

$$\frac{\partial J}{\partial t}=D\frac{\partial^2 J}{\partial r^2} \tag{31}$$

where the diffusivity is given by $D=cl_t/3$ [45], implying that in this limit $\mu_1=3^{-1/2}$.

Davis et al. [45] analytically solved a variant of Eq. (31) in which J is allowed to vary in all three dimensions, i.e. $\partial J/\partial t=D\nabla^2 J$, via a Fourier–Laplace transform. This yielded expressions for measurable quantities such as the fraction of light reflected (proportional to the vertical integral of the red or black lines in Fig. 16a) and the mean path-length in the cloud (essentially the e-folding distance of the exponential tail in Fig. 16a), as a function of the total optical depth and the physical depth of the cloud. This analytical approach was recently extended from a vertically homogeneous cloud to one in which the scattering properties were allowed to vary with height [84]. However, care must be taken in applying methods based on the diffusion approximation to radars such as CloudSat, since it is not straightforward to estimate a priori whether the measured signal is dominated by *MS* (for lidar in stratocumulus the dominance of *MS* is obvious). Another practical difficulty is that the instrument field-of-view does not appear explicitly in the [45] expressions, but has a strong effect on the shape of the exponential tail. Nonetheless, analytical approaches do provide insight into key processes at work and potentially provide benchmarks against which numerical techniques can be tested in idealized configurations.

5. Simulated *MS* effects for high frequency radars

Monte-Carlo codes have been widely used to investigate effects of *MS* for the 13.5–35 GHz GPM [20,85], for the 94 GHz CloudSat [86,19,87,76] and for the 94 GHz EarthCARE configuration [19] with focus on liquid precipitation. Very recently [88] studied *MS* effects in snow when observed by a CloudSat-like radar.

An example of such simulations is provided in Fig. 17 where the *SS* properties derived from the hurricane simulation of Fig. 2 are input for the radar received power simulations. Two configurations are here considered: a GPM-like K_u−band radar flying at 400 km altitude with a beam-width of 0.7° and a CloudSat *W*-band radar flying at 705 km altitude with a beam-width of 0.1°, which correspond to a 3-dB footprint radius of 2.45 and 0.65 km, respectively. While *MS* affects the TRMM-like radar only in the presence of extreme precipitation (compare left top and bottom panel of Fig. 17) particularly by producing pulse stretching below the surface (only visible at reflectivities below the noise level, profiles at distances around 50 to ~100 km and 200 to 250 km) it has a remarkable impact at 94 GHz: the *MS* signal becomes detectable in vast areas, which would result in returns below the noise threshold in the *SS* regime. Long pulse stretching below the surface is observed as well.

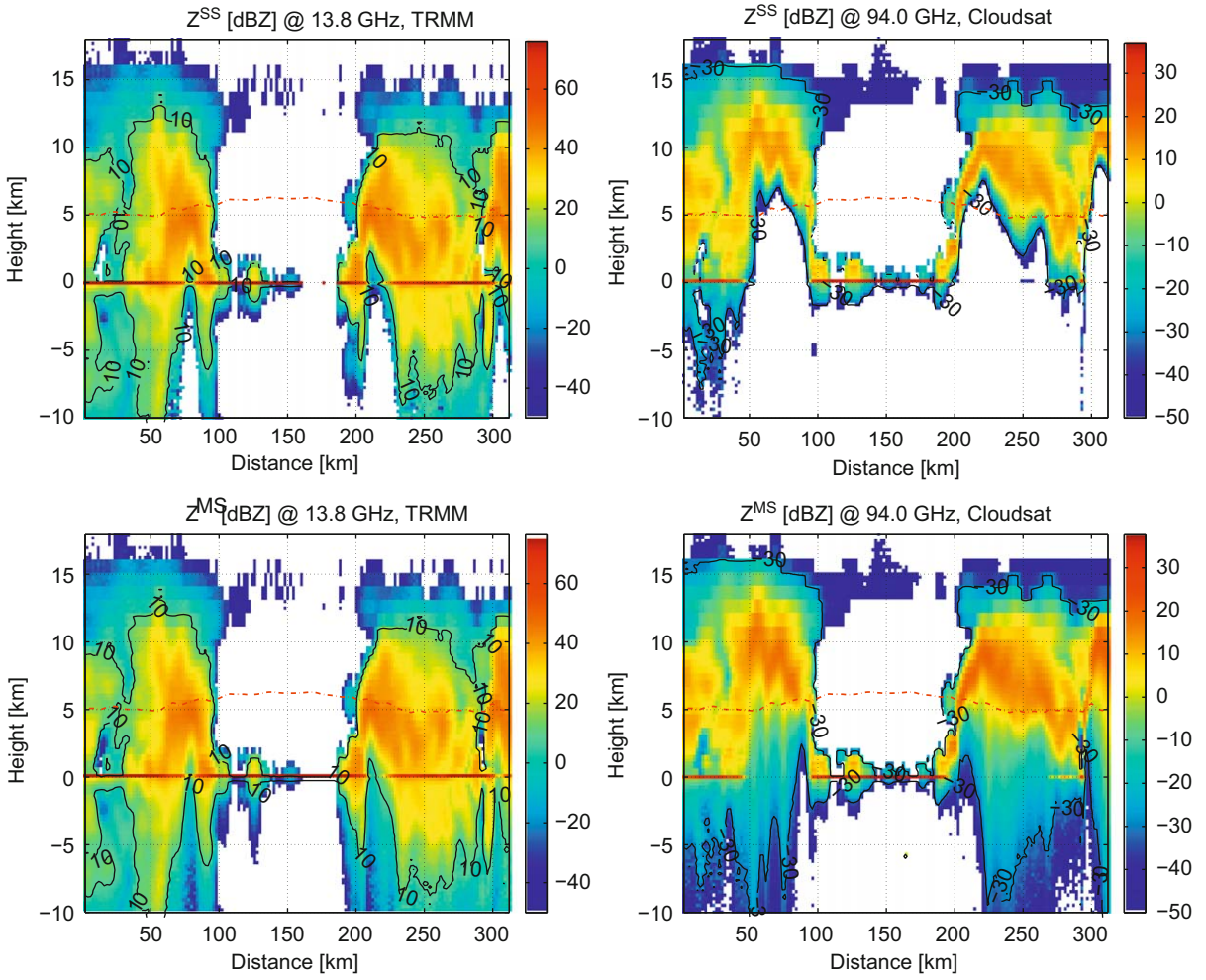

Fig. 17. *SS* (top) and *MS* reflectivities computed for a K_u GPM-like (left) and for the *W* CloudSat radar (right) corresponding to the *SS* propertied illustrated in Fig. 2. The *SS* panels include the mirror image contribution. The black contour indicates the noise level (dBZ_0) equal to 10 and -30 dBZ for the GPM and CloudSat radars. The dot-dashed line indicates the freezing level height.

This example confirms the findings of all the aforementioned authors, which can be summarized as follows:

1. In typical space-borne configuration the role of *MS* is increasingly important as the frequency progresses from K_u to *W* band (with simultaneous intensification of the scattering coefficient and reduction of the mean-free-path). At 13 GHz (TRMM/GPM configurations) the effect never exceeds a few dB even in the more extreme scenarios; at 35.5 GHz (GPM configuration) *MS* enhancement can reach tens of dB; in CloudSat configuration even profiles containing moderate rain rate ($\sim 3-5$ mm/h) are likely to be affected by *MS* at ranges close and crossing the surface-range.
2. *MS* effects can explain the absence of a surface-echo peak. For CloudSat the surface-range return is significantly contaminated by *MS* contributions at rain rates above 5/10 mm/h (depending on the system type, ice density and configuration) and it is certainly completely decoupled from the surface properties for rain rates above 15 mm/h. "Smooth" profiles at surface ranges are distinctive signatures of strong *MS* effects.
3. *MS* produces long signal tails at ranges below the surface, which lowers significantly the minimum detection height (even to tens of kilometers below the surface for 94 GHz systems).
4. In snow precipitating clouds the *MS* component expected for CloudSat observations can almost completely compensate for attenuation losses.
5. All *MS* effects in precipitating clouds are highly dependent on the presence of a thick scattering layer aloft. This is typically provided by large/dense ice particles above the melting layer which strongly enhance *MS*.

6. Evidence of MS in air-borne radar observations

Given the strong dependence of wide-angle *MS* on the ratio between footprint size and mean free path, *MS* effects

Please cite this article as: Battaglia A, et al. Multiple-scattering in radar systems: A review. JQSRT (2010), doi:10.1016/j.jqsrt.2009.11.024

(other than those involving surface scattering such as the three body scattering and the mirror image described in Section 3) can usually be neglected in ground- and air-borne weather radar applications. In fact, at the so-called non-attenuating radar frequencies (e.g. *X*-band and lower), which are used for ground-based precipitation radars, the mean free transport path is normally larger than the footprint, even for long range radars. Even at attenuating radar frequencies (e.g. from K_u- to *W*-band), in airborne applications and for ground based vertical profilers used for cloud studies, noticeable contributions by *MS* are rare due to the small cross-beam size. The fact that *MS* can usually be neglected in these applications, does not mean that it was ignored by the cloud and precipitation radar community. In depth analysis of specific features of the backscattered signal has provided sufficient evidence of *MS* effects involving multiple reflections between hydrometeors at frequencies as low as the *K*-band. The clearest cases have been observed by multi-frequency, polarimetric radars. In fact, *MS* signatures are intrinsically elusive for single-frequency non-polarimetric radars because they are noticeable only in high path attenuation cases; in these conditions, the ill-conditioned nature of single-frequency single-polarization radar retrievals is sufficient to cast a shadow of doubt on whatever scant evidence of this phenomenon is observed. On the contrary, when co-located radar profiles of reflectivity and depolarization at two or more frequencies are available, evidence of *MS* effects becomes less elusive. The work by [43], for example, stimulated much of the research in the subsequent decade (cited in this review). Only one example of a radar profile was documented there, but the clarity of the argument explaining the otherwise puzzling features by means of a theoretical model did not leave much room for doubt: *MS* effects had been observed in the field at K_a−band. The key clue in this kind of observation is the gradual increase (moving away from the radar) of depolarization signatures at the higher frequency, while the depolarization signature at the lower frequency does not increase.

Next we refer to an example (shown in Figs. 18 and 19 to document the rationale proposed in [43]. During the Wakasa Bay experiment in 2003, JPL's Airborne Precipitation Radar second generation (APR-2, [89]) was deployed on the NASA P-3 to support validation of the AMSR-E instrument. APR-2 is a cross-track scanning K_u-/K_a-band Doppler, polarimetric radar. On January 19th a frontal system south of Japan, including a well defined convective area and an associated wide stratiform precipitation area, was observed. In the transect of the system (Fig. 18) one can observe the following features.

- The typical linear depolarization ratio (*LDR*) signature is visible at both frequencies; it is generated by melting snowflakes in the bright band region at about 2.7 km. Whereas differences in the altitude of the peak value of *LDR* (i.e. less than 100 m) and in its magnitude have been used to infer properties of particles inside

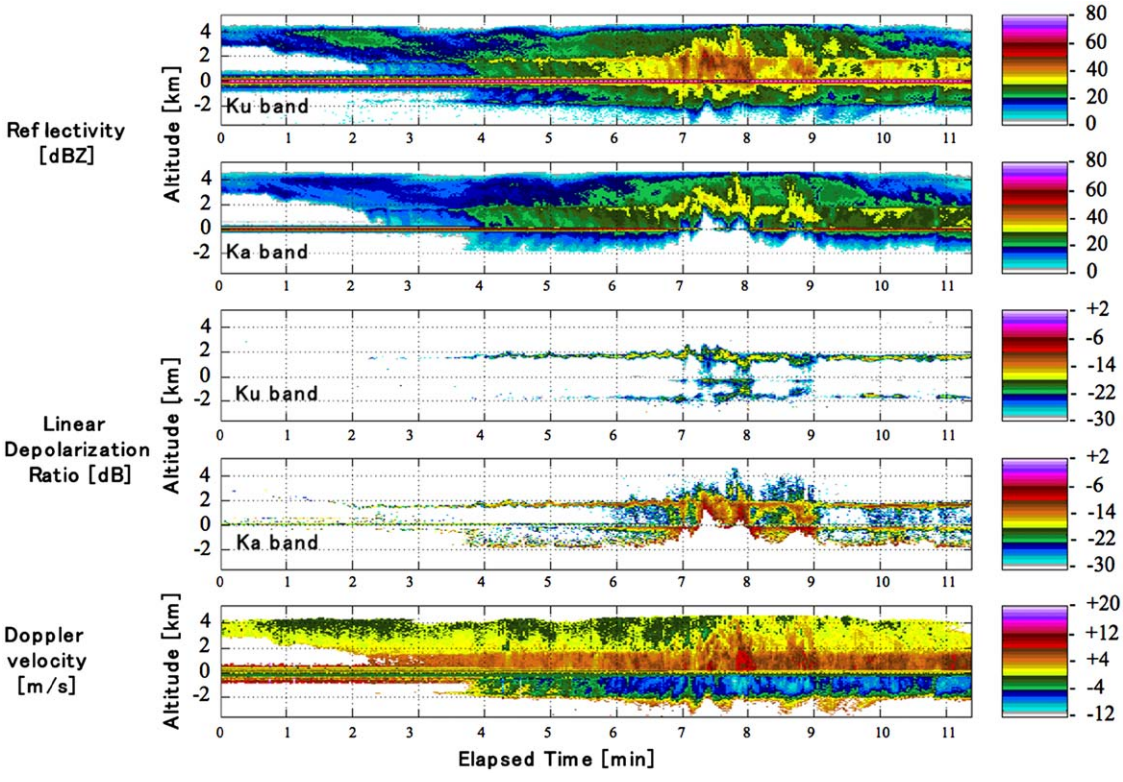

Fig. 18. Wakasa Bay Experiment Stratiform system with embedded convection—January 19th 2003 Flight #3. From 3230′*N*, 13630′*E* (at 04:05 UTC) to 3230′*N*, 13530′*E* (at 04:16 UTC).

the melting layer, the *LDR* profiles at K_u- and K_a-band are approximately collocated and correlated.

- The mirror image return appears at ranges below the surface on all channels (the mirror image is clearer in the K_u−band channels because of the lower path attenuation and higher surface normalized radar cross-section). Depolarizing effects induced by surface scattering are also evident in the *LDR* vertical sections.
- The *LDR* signature associated with intense precipitation and mixed phase particles in convective cores, shows the tell-tale signs of *MS* from 7 and 9 min of flight in this dataset.

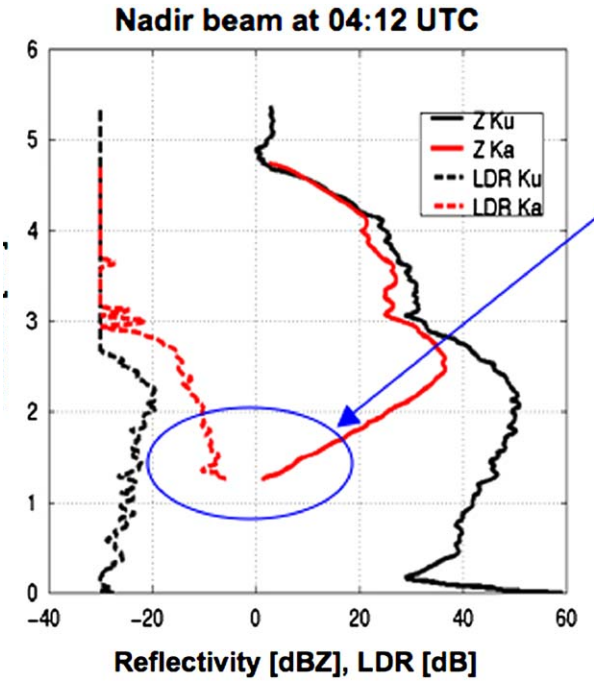

Fig. 19. Wakasa Bay Experiment. Dual frequency, dual polarization measurements of a convective area from the APR-2 showing evidence of *MS*.

The profile shown in Fig. 19 is extracted from that region. In this example, the K_u band *LDR* return shows a peak at 2.2 km altitude (corresponding to the melting layer altitude in the surrounding stratiform rain system) and slowly decreases below it. This behavior is typical of such cores and representative for the presence of large mixed phase hydrometeors below the freezing level due to convection. On the other hand, the K_a *LDR* return increases linearly below the melting layer altitude: just like in the example shown in [43] this depolarization signature is not actually generated by mixed phase hydrometeors (as shown by the K_u−band *LDR* profile), but by *MS* events in the high scattering region around the zero isotherm. This behavior is well captured by the *MS* models cited in this paper.

The launch of CloudSat has stimulated a second kind of multiparametric investigation of the *MS* effects in radar returns. In fact, airborne *W*-band radars have been used to validate CloudSat's *W*-band cloud profiling radar (CPR) mainly focusing on calibration, geolocation and detection skills. However, they have also served as experimental confirmation of the occurrence of *MS* in CPR's observations. The first reported case is shown in Fig. 20 [90]: in

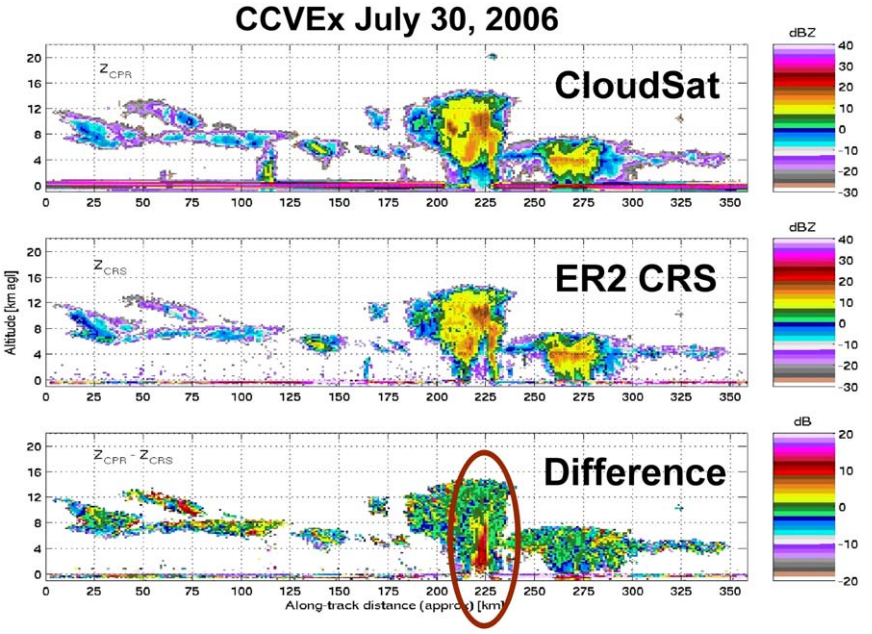

Fig. 20. Evidence of *MS* effects from the airborne CloudSat/CALIPSO Validation Experiment (CCVEx). Top panel: CloudSat radar reflectivity in dB*Z*; central panel: ER2-CRS radar reflectivity in dB*Z* under the CloudSat ground-track; bottom panel: difference between the CPR and the CRS reflectivities in dB. This image was generated using CRS preliminary calibration data courtesy of G. Heymsfield (NASA/GSFC) and L. Li (GEST). Relative calibration between CPR and CRS has been corrected since, and this image should be regarded as calibrated within 3 dB. The *MS* signature due to the different footprint sizes is evident well beyond this calibration bias. Extracted from [87].

Please cite this article as: Battaglia A, et al. Multiple-scattering in radar systems: A review. JQSRT (2010), doi:10.1016/j.jqsrt.2009.11.024

this vertical section, CPR measured reflectivity is compared to reflectivity measured by the GSFC/Cloud Radar System (CRS, [91]) on board NASA ER-2 aircraft. The exact time of co-location is highlighted by the NASA-ER-2 target signature visible in the CPR data. Most of the cloud and rainfall scene shows reflectivity values that are within the respective calibration and measurement uncertainties of the two radars. The region at the bottom of the convective core preceding the instant of Over-flight by less than a minute shows, however, a large positive bias in CPR's measurements versus CRS's. As predicted by pre-launch modeling efforts, and summarized herein, the discriminating factor in this case is the footprint size (1.4 km for CPR and less than 800 m for CRS). This, and other cases have been analyzed and documented (e.g. [87,92]) in support of the ongoing efforts aiming at improving CloudSat's forward modeling and cloud properties retrievals.

7. Evidence of MS in CloudSat observations

Evidence of *MS* is present in CloudSat 94 GHz CPR reflectivity profiles, showing features not interpretable in the frame of *SS* models or of the mirror image theory but fully explainable with *MS* theory.

1. For some overpasses over tall precipitating systems there is no "discontinuity" peak in the reflectivity signal at ranges corresponding to the surface; in exceptional cases, the reflectivity profiles exhibit extremely long tails at apparent ranges below the surface.
2. For precipitating profiles, which are likely to bear considerable quantity of rain, the vertical gradients of reflectivity are far-off the values expected from attenuated *SS* profiles.
3. The *PIA* estimated via the surface reference technique presents anomalous *pdf* s with a non-physical peak around 50 dB.

In the following subsections we briefly discuss these three aspects.

7.1. The quintessence of MS: second trip echoes in CloudSAT observations

An astonishing example of *MS* is provided by the CloudSat observation of a tropical storm at 06W on the 24 July 2006 (Fig. 21). In this case the pulse stretching extends beyond the unambiguous range interval so that the return appears as a second trip echo at the very top of the cloud, thus creating the bizarre signature above 18 km. The *CPR* has a pulse repetition frequency of 4300 Hz leading to a maximum unambiguous range of about 35 km.

In Fig. 22 we analyze in more detail one profile extracted from Fig. 21. The echo above 18 km represents the folding of the second trip echo; when unfolded it

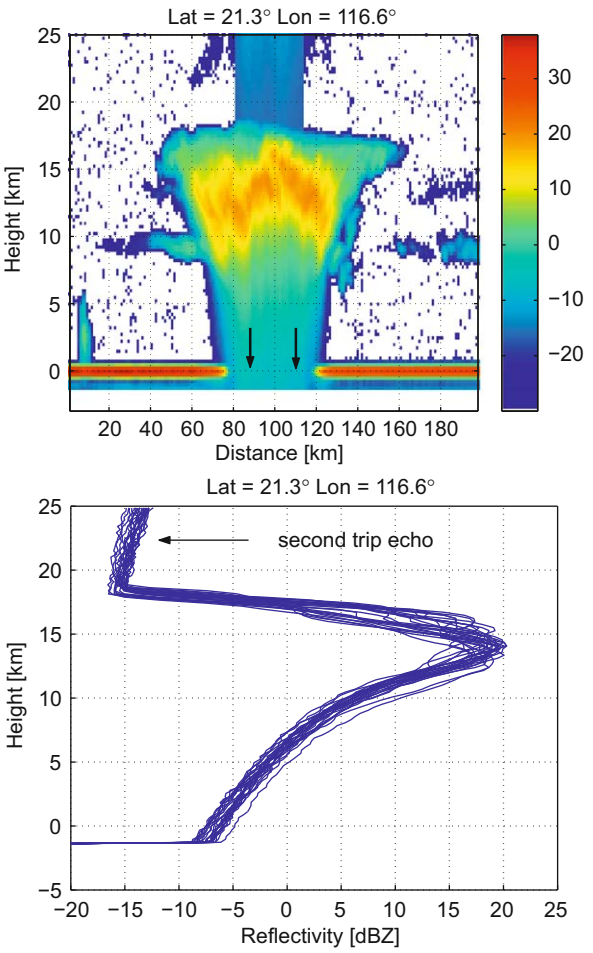

Fig. 21. Upper panel: CloudSat reflectivity vertical cross-section for a Tropical Storm 06W which occurred on the 24 July 2006 (granule 1272) south-west of Taiwan. Lower panel: vertical reflectivity profiles corresponding to the pixels between the two black arrows in the upper panel (extracted from [19]).

corresponds to a signal coming from ranges far below the surface (see double arrows in Fig. 22). The dashed line in Fig. 22 depicts the linearly interpolated-reconstructed profile for ranges below the surface (the 2B-GEOPROF product provides only the reflectivity for ranges at most 1.5 km below the surface as visible in Fig. 21. A best-matching procedure between the observed profile (Fig. 22) and a large dataset of simulated profiles [87] has been carried out. The best-matched profile is defined as the profile which minimizes the following cost function:

$$\sum_{j=1}^{N_{grids}} |Z_{CloudSAT}[j] - Z_{sim}^{MS}[j]| \tag{32}$$

where $Z_{CloudSAT}[j]$ and $Z_{sim}^{MS}[j]$ are the CloudSat measured and simulated reflectivity at grid point j. By visual inspection of Fig. 22, the simulated best-matched profile (circle line) not only fits quite well the CloudSat Z-signal

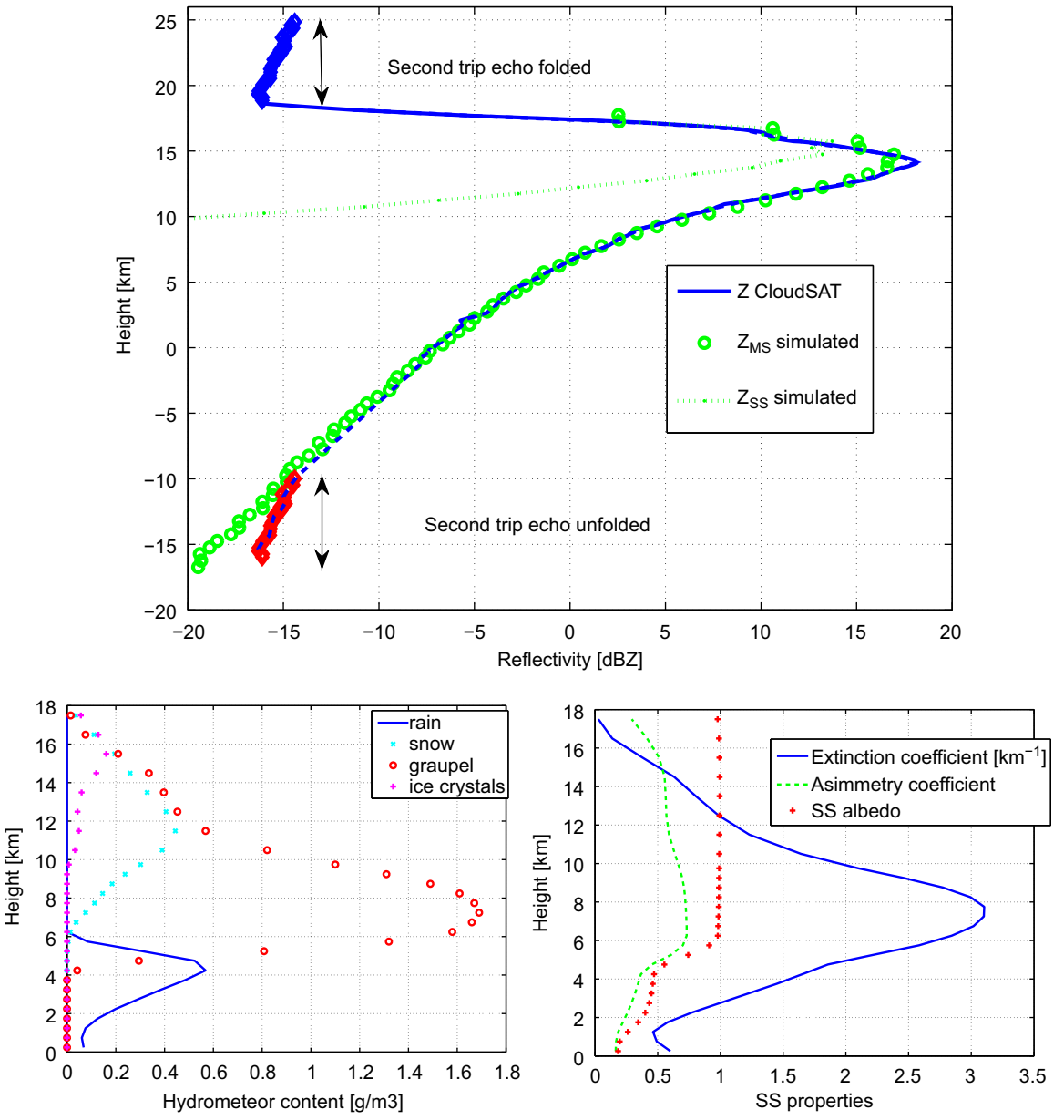

Fig. 22. Top panel: one of the CloudSat reflectivity profile extracted from the profiles depicted in the bottom panel of Fig. 21 with the best matching simulated profile and its *SS* counterpart. Bottom panels: hydrometeor content (left) and *SS* properties (right) corresponding to the simulated best matching profile of the top panel.

(continuous line) at apparent ranges above surface but also below it. The corresponding hydrometeor contents are extreme, particularly in the ice phase (e.g. the integrated graupel content reaches 10.2 kg/m^2), leading to a total optical thickness amounting to 24.5, i.e. to more than 200 dB two-way attenuation. Consequently, the *SS* profile of the best-matching profile (dotted line) is rapidly attenuated already at high altitudes. *SS* theory—even with the inclusion of the mirror image—cannot reproduce the peculiar features of this observation, which, therefore, can be considered the "par excellence" *MS* example.

7.2. Reduced height gradients of CloudSat reflectivity profiles

As already noticed in Section 5 the presence of *MS* tends to partly compensate for attenuation, thus reducing the height reflectivity gradient. This variable is particularly valuable for estimating rain profiles; [93] proposed an attenuation-based method to retrieve vertical profiles of rainfall rates from height derivatives of CloudSat nadir reflectivities. Assuming *SS* and the dominance of attenuation in shaping vertical trends of observed reflectivity (i.e. changes of measured reflectivity Z_{app} in rain at a

vertical interval are dominated by attenuation in rain, and not by the variability of non-attenuated reflectivity Z_{eff}), the one-way attenuation coefficient in rain $k_{ext}^{rain}(h)$ is estimated from the vertical gradient of the measured reflectivity, $\partial Z_{app}(z)/\partial z$, in a rain layer as

$$k_{ext}^{rain}(z) = \frac{1}{2}\frac{\partial Z_{app}(z)}{\partial z} - \mathcal{G}(z). \quad (33)$$

Here the coefficient $\frac{1}{2}$ accounts for the two-way propagation, and $\mathcal{G}(z)$ is the gaseous (O_2 and H_2O) absorption correction, which is determined by profiles of temperature, pressure, and relative humidity. Temperature and pressure profiles are available as auxiliary CloudSat information, $\mathcal{G}(z)$ being actually an output variable of the CloudSAT 2B-GEOPROF product. Because at 94 GHz the rain rate *RR* is approximately linearly dependent to k_{ext}^{rain} as

$$RR(z)[\mathrm{mm/h}] \approx 1.2\ \frac{1.1}{[\rho_a(z)]^{0.45}} k_{ext}^{rain}(z)\,[\mathrm{dB/km}] \quad (34)$$

ρ_a being the air density in kg/m^3, the combined use of Eqs. (33) and (34) can provide an estimate of *RR* profiles if *MS* effects are minor.

CloudSat data for June–July–August 2007 have been used to compute the value of k_{ext}^{rain} at an altitude of 1 km. Frequency distributions of this variable as a function of $\mathcal{I}_{>10\,\mathrm{dBZ}} \equiv \int_{Z>10\,\mathrm{dBZ}} Z_{app}(z)\,dz$ are plotted in Fig. 23. At low values of $\mathcal{I}_{>10\,\mathrm{dBZ}}$, where the *SS* theory is assumed to be valid, a large variety of k_{ext}^{rain} is encountered with the highest values corresponding approximately to 20 mm/h. Note that also negative values are registered, corresponding to situations where the non-attenuated reflectivity Z_{eff} is in fact decreasing with height. An increase in $\mathcal{I}_{>10\,dB}Z$, i.e. in the peak reflectivity of the hydrometeor and thus likely in the rain amount, drastically reduces the variability of k_{ext}^{rain} and of its maximum value. This is totally unexplainable within the frame of *SS* theory. At very high $\mathcal{I}_{>10\,dB}Z$, when the *MS* drives the whole process, the values of k_{ext}^{rain} never exceed few dB/km. This happens also to the reflectivity profiles (Fig. 21), which are characterized, close to the surface, by derivatives of the order of less than 1 dB/km, i.e. lower than the typical gas attenuation at 1 km height for a tropical atmosphere. A *SS* attenuation-based method would therefore predict no rain for the huge tropical system of Fig. 21, which is obviously not true. The Occam's razor favors again the straightforward *MS* interpretation: the increase of *MS* augments the in-cloud pulse stretching, decorrelates the signal with the hydrometeor content effectively present at 1 km altitude, and substantially dampens the reflectivity gradient at the same altitude.

7.3. Bimodal pdf of the path integrated attenuation and structure of surface precipitation

Two-way *PIA* s derived from surface-reference-technique (*SRT*) are shown in Fig. 24 for June–July–August 2007. Only profiles with freezing level above 4.5 km and flagged as "certain rain" according to the *Precip_flag* of the CloudSAT 2C-PRECIP-COLUMN product have been considered. The distribution exhibits a bimodal structure: the most frequent mode is characterized by low values of *PIA* with a peak near 3 dB, which is characteristic of light precipitation. The other mode, with peaks between 40 and 60 dB is most

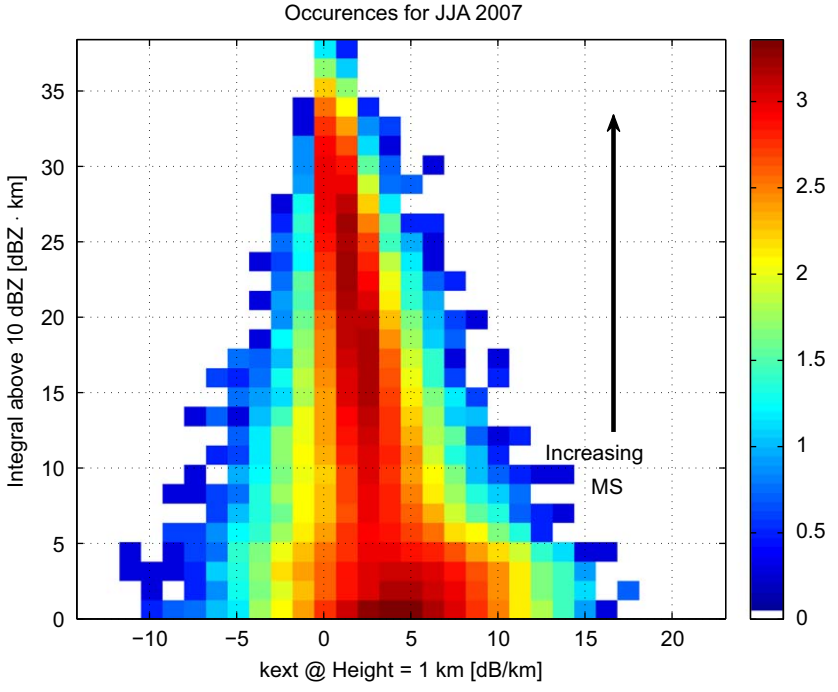

Fig. 23. Log_{10} of the number of occurrences (colorbar values) in the $(k_{ext}^{rain}, \mathcal{I}_{>10\,\mathrm{dBZ}})$ space. Profiles over sea with freezing level above 4.5 km identified as rainy in the 2C-PRECIP-COLUMN product and with two-way *PIA* above 25 dB have been considered. (For interpretation of the references to color in this figure legend, the reader is referred to the web version of this article.)

Please cite this article as: Battaglia A, et al. Multiple-scattering in radar systems: A review. JQSRT (2010), doi:10.1016/j.jqsrt.2009.11.024

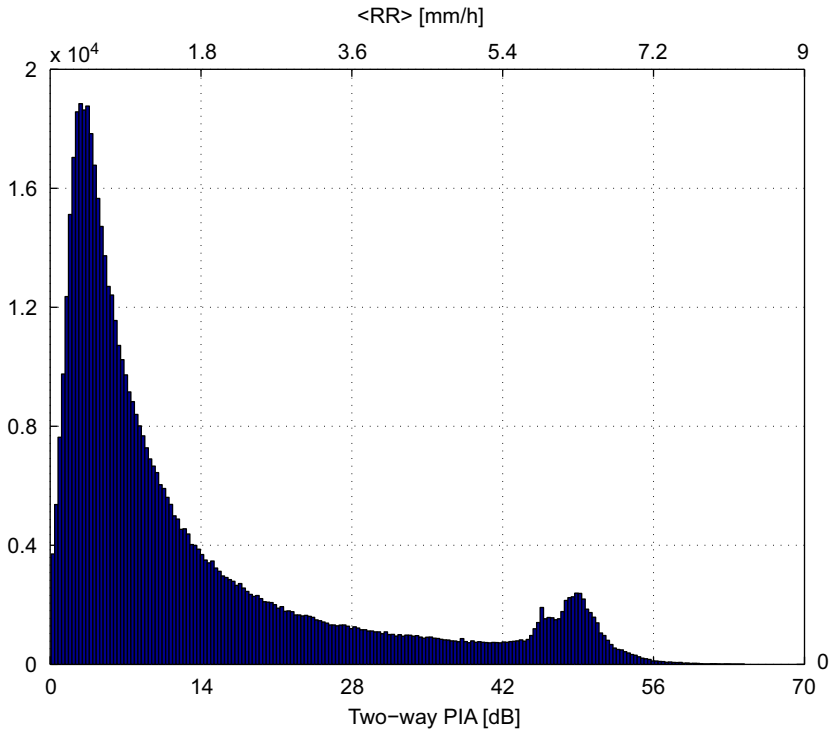

Fig. 24. Histogram distribution of *PIA* estimated from the *SRT*. The statistics refers to CloudSAT observations collected during JJA 2007 over sea with freezing level above 4.5 km identified as rainy in the 2C-PRECIP-COLUMN product.

pronounced in the western Pacific and Indian regions where deep convection is prevalent.

As a rule of thumb, the use of Eq. (34) with the assumption of a 5-km uniform rain layer and a mean density of 0.95 kg/m^3 leads to the estimate of the mean rain rate in the column as: $\langle RR \rangle_{layer}$ [mm/h] $\approx 1.35 \times PIA_{hydro}^{2-way}$ [dB]/10. This estimate is reported in the upper x-axis of Fig. 24. If *SS* approximation were valid, we would conclude that the frequency distribution of surface precipitation is bimodal in nature (as previously noted in [94]). As demonstrated in [19,87], Fig. 6, the coincidence between true and *SRT*-derived PIA_{hydro} is generally not fulfilled because of the saturation of the surface return signal due to *MS* effects. The apparent peak at about 7 mm/h actually includes profiles with much higher rain rates, whose ice segments are producing *MS* strong enough to significantly contaminate the surface return.

8. Identifying and accounting for MS in radar observations

The identification of *MS*-burdened profiles is quite challenging; a reflectivity enhancement can in general be masked by many other effects (e.g. size distribution and habit variability, unresolved attenuation or vertical variability effects, etc.). Battaglia et al. [85,86] (Figs. 15 and 9, respectively) demonstrated that a key parameter to forecast the total magnitude of the *MS* effect is provided by the scattering optical thickness. Unfortunately this parameter cannot be measured directly. It is essential to identify a proxy for *MS* by exploiting additional measurements, if available, or information coming from the vertical structure of the reflectivity profile.

Battaglia et al. [85,86] showed that *MS* effects manifest themselves by producing significant cross-talk. LDR_{hv}^{MS} (see definition in Eq. (23)) is much stronger than LDR_{hv}^{SS} and provides clear signatures with high *LDR* (up to 0 dB) in regions where high ΔZ_a^{MS} are located. Such effects have been confirmed by airborne observations (Section 6). The cross-polarized return power, which is unfortunately, very seldom available, represents a valuable proxy of *MS* effects and therefore could be a key quantity for incorporation into retrieval algorithms. For instance it is possible to select a threshold for the LDR_{hv} above which *MS* effects provide substantial change in the reflectivity (Fig. 14 in [85]).

Later [87] investigated the potential of the *PIA* estimated via *SRT* to flag CloudSat *MS*-affected profiles. This parameter, retrievable with sufficient precision only over sea, has been exploited to identify four *MS* regimes: (1) the *SS* approximation is applicable to the entire *Z*-profile; (2) the *SS* approximation is unreliable but the second order of scattering approximation is valid; (3) the second order of scattering approximation is not valid due to higher order of *MS* effects which do, however, not affect the *SRT*-based *PIA* estimates; (4) the *MS* is affecting the surface return as well, thus spoiling the *PIA* estimates. The PIA_{hydro} thresholds for identification of these regimes are listed in Table 1 in [87] for systems with different freezing level altitudes. For ocean pixels, about 80% (90%) of the profiles identified as rainy in the CloudSAT 2C-PRECIP-COLUMN product can be treated with the *SS* (*SOS*) approximation. For 3.5% of the rainy pixels even the *PIA*

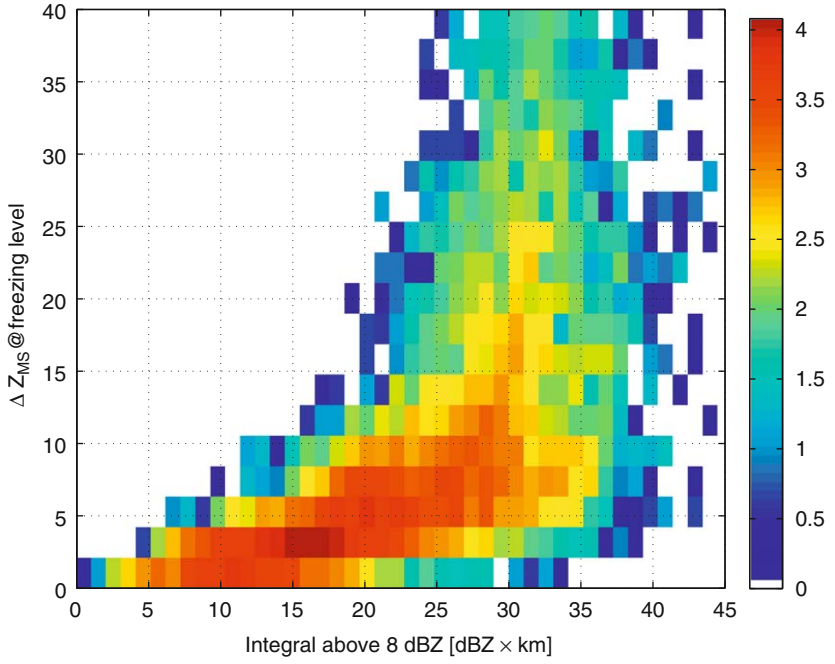

Fig. 25. Log_{10} of the number of occurrences (colorbar values) in the *MS* enhancement, $\mathcal{I}_{>8\,\mathrm{dBZ}}$ plane. Each simulated profile has a counterpart in a CloudSat observed profile. Only CloudSat profiles over sea with freezing level above 4.5 km, with two-way $PIA_{hydro} > 5$ dB and reaching the 5-dB*Z* level at altitude higher than 6 km have been considered.

estimate is unreliable. Due to the different precipitation regimes, the frequency with which *MS* effects are encountered is strongly region and season-dependent. Highest occurrences are in well developed and optically thick systems, frequently found in the InterTropical Convergence Zone and in the tracks of extra-tropical cyclones. These conclusions are particularly relevant to assessing the potential of space-borne 94 GHz radars for estimating precipitation on the ground.

Another key issue concerning 94 GHz space-borne radars is the identification of *MS* contaminated profiles at high altitudes, which has strong repercussions on estimates of ice water content in mesoscale convective systems. This has been raised first by [92] who, based on colocated CloudSat and RASTA 94 GHz air-borne radar measurements, reported a value of at least 2.5 dB *MS* enhancement in CloudSat observations at 8.5 km height in the anvil of a west-African mesoscale convective system sampled during the AMMA experiment. By exploiting long-term ground-based observations over Darwin quasi-spatially and temporally collocated with CloudSat over-passes, [95] showed that the CloudSat convective ice profiles can be used down to approximately 9 km height (or 4 km above the melting layer) without attenuation correction. They suggested that the CloudSat profiles in convective ice need to be corrected for attenuation by supercooled liquid water and ice aggregates/graupel particles and *MS* prior to their quantitative use. In Fig. 25 results of the *MS* enhancement at the freezing level height for CloudSat-simulated profiles are presented. Note that out of a large variety of simulated profiles from Cloud Resolving Models only those which have an almost perfect counterpart in CloudSat observations in terms of vertical reflectivity and *PIA* matching are considered here. Moreover, the matching procedure has been applied only to CloudSat profiles over sea with freezing levels above 4.5 km, two-way $PIA_{hydro} > 5$ dB and reaching the 5 dB*Z* level at altitude higher than 6 km. Hydrometeors producing backscattering above 8 dB*Z* are believed to be burdened by *MS*; because *MS* gradually increases with the scattering optical thickness the area subtended by the vertical reflectivity profile above this threshold ($\mathcal{I}_{>8\,\mathrm{dBZ}}$) is adopted as a proxy for *MS* and used as *x*-axis in Fig. 25. There is a clear trend of increasing ΔZ_{MS} with larger $\mathcal{I}_{>8\,\mathrm{dBZ}}$, but also a larger variability. Profiles with $\mathcal{I}_{>8\,\mathrm{dBZ}} > 20$ dB*Z* km (like that described in [92] or that of Fig. 22) are likely to be strongly affected by *MS* at altitudes close to the freezing level.

Another approach to correct the *MS* effects is to include fast-forward simulators accounting for *MS* effects in iterative retrieval algorithms (like the optimal estimation technique proposed by [96]). The time dependent two-stream method described in Section 4 has been now included in the QuickBeam package (description in [83]). Extended studies are urgently needed in this field.

9. Open issues and conclusions

Four complex challenges remain open for an all-encompassing quantification of *MS* effects:

1. *The development of a comprehensive theory to better quantify the backscattering enhancement for time-dependent problems, in geometries departing from the*

exact backscattering condition: It is difficult to quantify the effect on satellite observations of a departure from the exact backscattering angle introduced by the moving platform. The width of the backscattering cone depends on how the signal is sampled in time as well as on the transport mean free path in precipitation/clouds. As a consequence, the radar measures a convoluted combination of diffuse and coherent *MS*.

2. *The evaluation of simulated MS effects by more direct ad-hoc measurements*: Particularly useful in this context would be air-borne radar measurements of precipitation performed with a receiving system consisting of several antennas of different sizes; this set-up could produce many more case studies than the few collected during satellite under-flights (Section 6). The signal received at the smaller antenna (thus corresponding to a larger footprint) should be affected by *MS* while that of the large antennas should be designed to provide the *SS* reference level. A full verification of radar *MS* effects would greatly benefit from simultaneous measurements of *LDR* and sampling the signal from apparent ranges far below the surface. These specifics/configurations are therefore suggested for next air-borne validation campaigns related to high-frequency space-borne missions.
3. *The assessment of the impact of MS in Doppler high frequency radars foreseen for up-coming space-missions, primarily EarthCARE*: Up to now, theoretical investigations involving Doppler space-borne radars focused on the effects of non-uniform beam filling on vertical rainfall velocity measurements [97,98] and of errors induced by pointing uncertainties [99]. The presence of *MS* with spurious velocity signals coming from higher order scattering is expected to further degrade the signal, both biasing the mean and widening the spectral width. No forward model is currently available to simulate such features.
4. *The inclusion of MS corrections into data assimilation and retrieval algorithms*: Instead of flagging the profiles burdened by *MS* and avoiding their use in deriving cloud and precipitation products (with possible introduction of undesired biases), an interesting but largely unexplored avenue of research involves the application of pulse stretching and *MS* data to derive cloud and precipitation *SS* properties (extinction, bulk scattering phase function). The exploitation in data assimilation and in retrieval procedures of fast forward operator inclusive of *MS* would certainly pursue this goal.

Acknowledgements

The work performed by Dr. Battaglia has been partially funded by the German Science Foundation under the TOSCA project. The contribution by Dr. Simone Tanelli was performed at the Jet Propulsion Laboratory, California Institute of Technology under contract with the National Aeronautics and Space Administration. Dr. Valery Melnikov maintained calibration of the NOAA/NSSL polarimetric radar and collected data, whereas Jelena Andric produced Figures 8–10.

References

[1] Doviak RJ, Zrnić DS. Doppler radar and weather observations, 2nd ed. Mineiola, NY: Dover; 2006.
[2] Bringi VN, Chandrasekar V. Polarimetric doppler weather radar, principles and applications. Cambridge: Cambridge University Press; 2001 p. 636.
[3] Kummerow CD, Barnes W, Kozu T, Shiue J, Simpson J. The tropical rainfall measuring mission (TRMM) sensor package. J Atmos Ocean Technol 1998:809–17.
[4] Tao W, Lang S, Olson W, Meneghini R, Yang S, Simpson J, et al. Retrieved vertical profiles of latent heat release using TRMM rainfall products for February 1998. J Appl Meteorol 2001;40:957–982.
[5] Stephens GL, Vane DG, Boain RJ, Mace GG, Sassen K, Wang Z, et al. The CLOUDSAT mission and the A-train. Bull Am Met Soc 2002;83(12):1771–90.
[6] Suzuki K, Stephens GL. Global identification of warm cloud microphysical processes with combined use of A-Train observations. Geophys Res Lett 2008; 35 (L08805), doi: 10.1029/2008GL033590.
[7] Luo Z, Stephens GL, Emanuel KA, Vane DG, Tourville N, Haynes J. On the use of CloudSat and data for estimating hurricane intensity. IEEE Geosci Remote Sens Lett 2008;5(1):13–6.
[8] Tao W-K, Simpson J, Baker D, Braun S, Chou M, Ferrier B, et al. Microphysics radiation and surface processes in the Goddard Cumulus Ensemble (GCE) model. Meteorol Atmos Phys 2003;82:97–137.
[9] Gasiewski A. Microwave radiative transfer in hydrometeors. In: Atmospheric remote sensing by microwave radiometry. New York: Wiley; 1993. p. 91–144.
[10] Eloranta EW. Practical model for the calculation of multiply scattered lidar returns. Appl Opt 1998;37:2464–72.
[11] Bissonnette LR. Lidar and multiple scattering. In: Weitkamp C, editor. Lidar range-resolved optical remote sensing of the atmosphere. Berlin: Springer; 2005. p. 43–104.
[12] Nicolas F, Bissonnette LR, Flamant PH. Lidar effective multiple-scattering coefficients in cirrus clouds. Appl Opt 1997;36:3458–68.
[13] Hogan RJ. Fast lidar and radar multiple-scattering models: part I: small-angle scattering using the photon variance–covariance method. J Atmos Sci 2008;65:3621–35, doi: 10.1175/2008JAS2643.1.
[14] van de Hulst HC. Light scattering by small particles. New York: Wiley-Interscience; 1981.
[15] Liou KN. An introduction to atmospheric radiation, second ed. New York: Academic Press; 2002.
[16] Bissonnette LR. Multiple-scattering lidar equation. Appl Opt 1996;35(33):6449–65.
[17] Miller SD, Stephens GL. Multiple scattering effects in the lidar pulse stretching problem. J Geophys Res 1999;104(D18):22205–19.
[18] Mahesh JDSDD, Eloranta AE. Atmospheric multiple scattering effects on GLAS altimetry—part II: analysis of expected errors in Antarctic altitude measurements. IEEE Trans Geosci Remote 2002;40:2353–62.
[19] Battaglia A, Simmer C. How does multiple scattering affect the spaceborne W-band radar measurements at ranges close to and crossing the sea-surface range?. IEEE Trans Geosci Remote Sens 2008;46(6):1644–51.
[20] Marzano FS, Roberti L, Di Michele S, Mugnai A, Tassa A. Modeling of apparent radar reflectivity due to convective clouds at attenuating wavelengths. Radio Sci 2003;38(1):1002, doi: 10.1029/2002RS002613.
[21] Marzano FS, Ferrauto G. Relation between weather radar equation and first-order backscattering theory. Atmos Chem Phys 2003;3:813–21.
[22] Zrnić DS. Three-body scattering produces precipitation signatures of special diagnostic value. Radio Sci 1987;22:76–86.
[23] Bohren CF, Huffman DR. Absorption and scattering of light by small particles. New York: Wiley; 1983.
[24] Battaglia A, Ajewole MO, Simmer C. Evaluation of radar multiple scattering effects from a GPM perspective. Part I: model description and validation. J Appl Meteorol 2006;45(12):1634–47.
[25] Wilson JW, Reum D. The flare echo: reflectivity and velocity signature. J Atmos Ocean Technol 1988;5(2):197–205.
[26] Lemon LR. The radar "three-body scatter spike": an operational large-hail signature. Weather Forecasting 1998;13(2):327–40.
[27] Hubbert J, Bringi VN. The effects of three-body scattering on differential reflectivity signatures. J Atmos Ocean Technol 2000;17:51–61.

Please cite this article as: Battaglia A, et al. Multiple-scattering in radar systems: A review. JQSRT (2010), doi:10.1016/j.jqsrt.2009.11.024

[28] Lindley T, Lemon L. Preliminary observations of weak three body scattering spikes associated with low and severe hail, E Journal of Severe Storms Meteorology 2007; 2 (3), 〈http://www.ejssm.org/ojs/index.php/ejssm/article/viewArticle/12/22〉.
[29] Ulaby FT, Moore RK, Fung AK. Microwave remote sensing active and passive, vol. 3. Norwood, MA: Artech House; 1990.
[30] Meneghini R, Atlas D. Simultaneous ocean cross section and rainfall measurements from space with a nadir-looking radar. J Atmos Ocean Technol 1986;3(3) doi: 10.1175/1520-0426(1986)003.
[31] Liao L, Meneghini R, Iguchi T. Simulations of mirror image returns of air/space-borne radars in rain and their applications in estimating path attenuation. IEEE Trans Geosci Remote 1999;37(2):1107–21.
[32] Li J, Nakamura K. Characteristics of the mirror image of precipitation observed by the TRMM precipitation radar. J Atmos Ocean Technol 2002;19(2):145–58, doi: 10.1175/1520-0426(2002)019.
[33] Li J, Nakamura K. Vertical distribution of the mirror image returns observed by TRMM PR and estimated for a 35-GHz radar. J Atmos Ocean Technol 2005;22(11):1829–37.
[34] Olson WS, Bauer P, Viltard NF, Johnson DE, Tao W, Meneghini R, et al. A melting layer model for passive/active microwave remote sensing applications. Part I: model formulation and comparison with observations. J Appl Meteorol 2001;48(7):1145–63.
[35] Bissonnette LR, Roy G, Roy N. Multiple-scattering-based lidar retrieval: method and results of cloud probings. Appl Opt 2005;44:5565–81.
[36] Cahalan RF, Oreopoulos L, Marshak A, Evans KF, Davis A, Pincus R, et al. The international intercomparison of 3D radiation codes (I3RC): bringing together the most advanced radiative transfer tools for cloudy atmospheres. Bull Am Met Soc 2005;86:1275–93.
[37] Oreopoulos L, Marshak A, Cahalan RF, Varnai T, Davis AB, Macke A. New directions in the radiative transfer of cloudy atmospheres. EOS 2006;87(5).
[38] Várnai T, Cahalan RF. Modeling and analysis of offbeam lidar returns from thick clouds, snow, and sea ice. In: International conference on mathematics, computational methods and reactor physics, Saratoga Springs, NY, May 3–7, 2009.
[39] Tsang L, Kong JA, Shin RT. Theory of microwave remote sensing. New York: Wiley-Interscience; 1985 ISBN 0-471-88860-5.
[40] Kobayashi S, Tanelli S, Im E. Second-order multiple-scattering theory associated with backscattering enhancement for a millimeter wavelength weather radar with a finite beam width. Radio Sci 2005;40:RS6015, doi: 10.1029/2004RS003219.
[41] Kobayashi S, Oguchi T, Tanelli S, Im E. Backscattering enhancement on spheroid-shaped hydrometeors: considerations in water and ice particles of uniform size, and Marshall–Palmer distributed rains. Radio Sci 2007;2(42):RS2001, doi: 10.1029/2006RS003503.
[42] Oguchi T, Ihara T. Computer simulation of enhanced backscattering from randomly distributed spherical scatterers at 30 GHz and comparison with measurement. Radio Sci 2006; doi: 10.1029/2006RS003468.
[43] Ito S, Oguchi T, Iguchi T, Kumagai H, Meneghini R. Depolarization of radar signals due to multiple scattering in rain. IEEE Trans Geosci Remote Sens 1995;33:1057–62.
[44] Oguchi T, Ishida N, Ihara T. Effect of multiple scattering on the estimation of rainfall rates using dual-wavelength radar techniques. IEEE Trans Geosci Remote Sens 1994;32(5):943–6.
[45] Davis AB, Cahalan RF, McGill MJ, Love SP. Offbeam lidar: an emerging technique in cloud remote sensing based on radiative green function theory in the diffusion domain. Phys Chem Earth 1999:177–85 (Erratum 757–765).
[46] Battaglia A, Ajewole MO, Simmer C. Multiple scattering effects due to hydrometeors on precipitation radar systems. Geophys Res Lett 2005;32:L19801, doi: 10.1029/2005GL023810.
[47] Ito S, Kobayashi S, Oguchi T. Multiple scattering formulation of pulsed beam waves in hydrometeors and its application to millimeter wave weather radar. IEEE Geosci Remote Sens Lett 2007;4:13–7.
[48] Kobayashi S, Ito S, Tanelli S, Oguchi T, Im E. A time-dependent multiple scattering theory for a pulsed radar with a finite beam width. Radio Sci 2007(42):RS4001, doi: 10.1029/2006RS003555.
[49] Hogan RJ, Battaglia A. Fast lidar and radar multiple-scattering models: Part 2: wide-angle scattering using the time-dependent two-stream approximation. J Atmos Sci 2008;65:3636–51, doi: 10.1175/2008JAS2643.1.
[50] de Wolf D. Electromagnetic reflection from an extended medium: cumulative forward scatter single-backscatter approximation. IEEE Trans Antennas Propag 1971;19:254–62.
[51] Kuga Y, Ishimaru A. Retroreflectance from a dense distribution of spherical particles. J Opt Soc A 1984;1(8):831–5.
[52] Barabanenkov Y, Kravtsov Y, Ozrin V, Saichev A. Enhanced backscattering—the universal wave phenomenon. Proc IEEE 79(10):1991;1367–70.
[53] Ishimaru A. Backscattering enhancement: from radar cross sections to electron and light localizations to rough surface scattering. IEEE Antennas Propag Mag 1991; 33 (5).
[54] Tsang L, Ishimaru A. Theory of backscattering enhancement of random discrete isotropic scatterers based on the summation of all ladder and cyclical terms. J Opt Soc Am A Opt Image Sci 1985;2:1331–8.
[55] Tsang L, Kong JA. Scattering of electromagnetic waves: advanced topics. New York: Wiley; 2001 p. 359–405 [chapter 8].
[56] Kobayashi S, Tanelli S, Iguchi T, Im, E. Backscattering enhancement with a finite beam width for millimeter-wavelength weather radars. In: Jackson GS, Uratsuka S. editors. Proceedings of SPIE. Microwave remote sensing of the atmosphere and environment IV, vol. 5654. 2004. p. 106–13.
[57] Mandt CE, Tsang L, Ishimaru A. Copolarized and depolarized backscattering enhancement of random discrete scatterers of large size based on second-order ladder and cyclical theory. J Opt Soc Am A 1990;7:585–92.
[58] Kuga Y. Depolarization effects of the enhanced retroreflectance from a dense distribution of spherical particles. JOSA Commun 1985;2(4):616–8.
[59] Ihara T, Oguchi T, Tazaki T. Measurement of backscattering enhancement due to random particles at 30 GHz band using mirror image technique. In: Proceedings of the URSI Commission F Open Symposium, Cairns, Australia, 2004. p. 59–64.
[60] Oguchi T. Effect of incoherent scattering on attenuation and cross polarization of millimeter wave due to rain: preliminary calculations at 34.8 GHz and 82 GHz for spherical raindrops. J Radio Res Lab 1980;27:1–51.
[61] Mishchenko MI. Enhanced backscattering of polarized light from discrete random media: calculations in exactly the backscattering direction. J Opt Soc Am A 1992;9:978–82.
[62] van Albada MP, Lagendijk A. Vector character of light in weak localization: spatial anisotropy in coherent backscattering from a random medium. Phys Rev B 1987;36:2353–6.
[63] Ishimaru A. Wave propagation and scattering in random media. New York: IEEE Press; 1997. p. 147–74 [chapters 7 and 8].
[64] Pruppacher HR, Pitter RL. A semi-empirical determination of the shape of cloud and rain drops. J Atmos Sci 1971;28:86–94.
[65] Oguchi T. Electromagnetic wave propagation and scattering in rain and other hydrometeors. Proc IEEE 1983;71:1029–78.
[66] van Albada MP, van der Mark M, Lagendijk A. Observations of weak localization of light in a finite slab: anisotropy effects and light-path classification. Phys Rev Lett 1987;58:361–4.
[67] Ishimaru A. Wave propagation and scattering in random media. New York, NY: Academic Press; 1978.
[68] Hong ST, Ishimaru A. Two-frequency mutual coherence function, coherent bandwidth, and coherence time of millimeter and optical waves in rain, fog, and turbulence. Radio Sci 1976;11:551–9.
[69] Ito S, Oguchi T. Circular depolarisation ratio of radar returns from rain: validity of the second-order solution of rt equation. IEEE Proc Microwave Antennas Propag 1994;141:257–60.
[70] Mishchenko MI, Travis LD, Lacis AA. Multiple scattering of light by particles: radiative transfer and coherent backscattering. Cambridge: Cambridge University Press; 2006.
[71] Bissonnette LR, Bruscaglioni P, Ismaelli A, Zaccanti G, Cohen A, Benayahu Y, et al. Lidar multiple scattering from clouds. Appl Phys B 1995;60:355–62.
[72] Hu Y-X, Winker D, Yang P, Baum B, Poole L, Vann L. Identification of cloud phase from PICASSO-CENA lidar depolarization: a multiple scattering sensitivity study. J Quant Spectrosc Radiat Transfer 2001;70(4–6):569–79.
[73] Battaglia A, Mantovani S. Forward Monte Carlo computations of fully polarized microwave radiation in non isotropic media. J Quant Spectrosc Radiat Transfer 2005;95(3):285–308.
[74] Labonnote LC. A 3d polarized Monte Carlo code: first results. In: International radiation symposium 2008, Foz Do Iguacu, Brazil, August 4–10, 2008.
[75] Battaglia A, Kobayashi S, Tanelli S, Im E, Simmer C. Multiple scattering effects in pulsed radar systems: an intercomparison study. J Atmos Ocean Technol 2008; 25 (9), doi:10.1175/2008JTECHA1023.1.
[76] Haynes JM, L'Ecuyer T, Stephens GL, Miller SD, Mitrescu C, Wood NB, et al. Rainfall retrieval over the ocean with spaceborne

Please cite this article as: Battaglia A, et al. Multiple-scattering in radar systems: A review. JQSRT (2010), doi:10.1016/j.jqsrt.2009.11.024

W-band radar. J Geophys Res 2008;114:D00A22, doi: 10.1029/2008JD009973.
[77] Lee L, Jokipii JR. Strong scintillations in astrophysics, ii, a theory of temporal broadening of pulses. Astrophys J 1975;201:532–43.
[78] Oguchi T, Ito S. Multiple scattering effects on the transmission and reflection of millimeter pulse waves in rain. Radio Sci 1990;25(3):205–16.
[79] Meador WE, Weaver WR. Two-stream approximations to radiative transfer in planetary atmospheres: a unified description of existing methods and a new improvement. J Atmos Sci 1980;37:630–643.
[80] Stephens GL, Gabriel PM, Partain PT. Parameterization of atmospheric radiative transfer—1. Validity of simple models. J Atmos Sci 2001;58:3391–409.
[81] Shonk JKP, Hogan RJ. Tripleclouds: an efficient method for representing cloud inhomogeneity in 1D radiation schemes by using three regions at each height. J Climate 2008;21:2352–70.
[82] Chandrasekhar S. Radiative transfer. New York: Dover Publications; 1960.
[83] Haynes JM, Marchand RT, Luo Z, Bodas-Salcedo A, Stephens GL. A multipurpose radar simulation package: QuickBeam. Bull Am Met Soc 2007;88(11):1723–7, doi: 10.1175/BAMS-88-11-1723.
[84] Davis AB. Multiple-scattering lidar from both sides of the clouds: addressing internal structure. J Geophys Res 2008;113:D14S10, doi: 10.1029/2007JD009666.
[85] Battaglia A, Ajewole MO, Simmer C. Evaluation of radar multiple scattering effects from a GPM perspective. Part II: model results. J Appl Meteorol 2006;45(12):1648–64.
[86] Battaglia A, Ajewole MO, Simmer C. Evaluation of radar multiple scattering effects in CloudSat configuration. Atmos Chem Phys 2007;7:1719–30.
[87] Battaglia A, Haynes JM, L'Ecuyer T, Simmer C. Identifying multiple-scattering affected profiles in CloudSat observations over the oceans. J Geophys Res 2008;113:D00A17, doi: 10.1029/2008JD009960.
[88] Matrosov SY, Battaglia A. Influence of multiple scattering on CloudSat measurements in snow: a model study. Geophys Res Lett 2009;36:L12806, doi: 10.1029/2009GL038704.
[89] Sadowy GA, Berkun AC, Chun W, Im E, Durden SL. Development of an advanced airborne precipitation radar. Microwave J 2003;46(1):84–98.
[90] Tanelli S, Im E, Durden S, Pak K. In-flight performance of the cloudsat radar & l1b processing. In: CloudSat/CALIPSO joint science team meeting, June 11–14, San Francisco, CA, USA, 2007.
[91] Li L, Heymsfield GM, Racette PE, Tian L, Zenker E. A 94-GHz cloud radar system on a NASA high-altitude ER-2 aircraft. J Atmos Ocean Technol 2004;21(9):1378–88.
[92] Bouniol D, Protat A, Plana-Fattori A, Vinson J-P, Giraud M, Grand N. Comparison of airborne and spaceborne 95 GHz radar reflectivities and evidence of multiple scattering in CloudSat measurements. J Atmos Ocean Technol 2008;25(11):1983–95, doi: 10.1175/2008JTECHA1011.1.
[93] Matrosov SY, Battaglia A, Rodriguez P. A method for estimating rainfall rates from height derivatives of CloudSat measurements. J Atmos Ocean Technol 2008;25(12):2199–208, doi: 10.1175/2008JTECHA1095.1.
[94] Haynes JM, Stephens GL. Tropical ocean cloudiness and the incidence of precipitation: early results from CloudSat. Geophys Res Lett 2007;34:L09811, doi: 10.1029/2007GL029335.
[95] Protat A, Bouniol D, Delanoë J, May PT, Plana-Fattori A, Hasson A, et al. Assessment of CloudSat reflectivity measurements and ice cloud properties using ground-based and airborne cloud radar observations. J Atmos Ocean Technol 2009;26(9):1717–41, doi: 10.1175/2009JTECHA1246.1.
[96] L'Ecuyer TS, Stephens GL. An estimation-based precipitation retrieval algorithm for attenuating radars. J Appl Meteorol 2002;41(3):272–85.
[97] Tanelli S, Im E, Durden SL, Facheris L, Giuli D, Smith E. Rainfall Doppler velocity measurements from spaceborne radar: overcoming nonuniform beam filling effects. J Atmos Ocean Technol 2004;21(1):27–44, doi: 10.1175/1520-0426.
[98] Schutgens NAJ. Simulated doppler radar observations of inhomogeneous clouds: application to the EarthCARE space mission. J Atmos Ocean Technol 2008;25(9):1514–28, doi: 10.1175/2007JTECHA1026.1.
[99] Tanelli S, Im E, Mascelloni SR, Facheris L. Spaceborne Doppler radar measurements of rainfall: correction of errors induced by pointing uncertainties. J Atmos Ocean Technol 2005;22(11):1676–90, doi: 10.1175/JTECH1797.1.
[100] Stephens GL, Austin RT. Airborne cloud radar (ACR) reflectivity, Wakasa Bay, Japan. Boulder, CO: National Snow and Ice Data Center. Digital media; 2004.

Please cite this article as: Battaglia A, et al. Multiple-scattering in radar systems: A review. JQSRT (2010), doi:10.1016/j.jqsrt.2009.11.024